ACSNANO

www.acsnano.org

ARTICLE

Prevent and Reverse Metabolic Dysfunction-Associated Steatohepatitis and Hepatic Fibrosis via mRNA-Mediated Liver-Specific Antibody Therapy

Chenshuang Zhang, Yilong Teng, Xin Bai, Maoping Tang, William Stewart, Jake Jinkun Chen, Xiaoyang Xu,* and Xue-Qing Zhang*

Cite This: https://doi.org/10.1021/acsnano.4c13404

Read Online

ACCESS | Metrics & More | Article Recommendations | Supporting Information

ABSTRACT: Chronic exposure of the liver to multiple insults culminates in the development of metabolic dysfunction-associated steatohepatitis (MASH), a complicated metabolic syndrome characterized by hepatic steatosis and inflammation, typically accompanied by progressive fibrosis. Despite extensive clinical evaluation, there remain challenges in MASH drug development, which are primarily due to unsatisfactory efficacy and limited specificity. Strategies to address the unmet medical need for MASH with fibrosis before it reaches the irreversible stage of decompensated cirrhosis are critically needed. Herein, we developed an mRNA-mediated liver-specific antibody therapy for MASH and hepatic fibrosis using a targeted lipid nanoparticle (LNP) delivery system. When encapsulated with IL-11 single-chain variable fragment (scFv)-encoded mRNA, the targeted AA3G LNP (termed m*IL11-scFv*@AA3G) specifically accumulated in the liver and secreted IL-11 scFv to neutralize overexpressed IL-11 in hepatic environments, thus inhibiting the IL-11 signaling pathway in hepatocytes and hepatic stellate cells. As a preventative regimen, systemic administration of m*IL11-scFv*@AA3G reversed MASH and prevented the progression to fibrosis in a murine model of early MASH. Notably, m*IL11-scFv*@AA3G exhibited superior efficacy compared to systemic administration of IL-11 scFv alone, attributed to the sustained antibody expression in the liver, which lasted 18-fold longer than that of IL-11 scFv. When tested in the MASH model with fibrosis, m*IL11-scFv*@AA3G effectively ameliorated steatosis and resolved fibrosis and inflammation. These findings present a versatile LNP platform targeting liver cell subtypes for the sustained expression of therapeutic antibodies to treat MASH and fibrosis. The developed mRNA-mediated liver-specific antibody therapy offers a promising approach for addressing MASH and holds the potential for expansion to various other diseases.

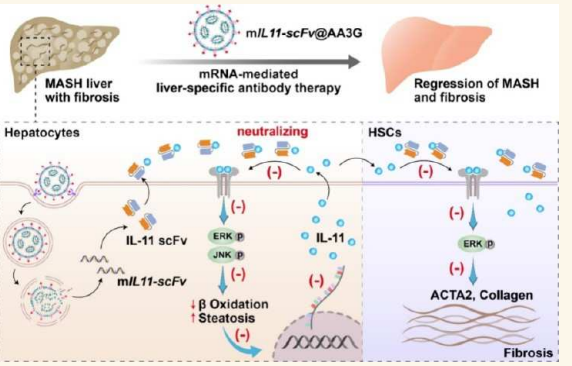

KEYWORDS: *lipid nanoparticles, targeted delivery, mRNA-mediated antibody therapy, metabolic dysfunction-associated steatohepatitis, liver fibrosis*

INTRODUCTION

Metabolic dysfunction-associated steatohepatitis [MASH, previously named nonalcoholic steatohepatitis (NASH)] is a severe progressive subtype of metabolic dysfunction-associated steatotic liver disease [MASLD, or previously nonalcoholic fatty liver disease (NAFLD)] that affects approximately 5% of the global population and occurs frequently with type 2 diabetes (T2D) and obesity.[1−3] Chronic exposure of the liver to multiple insults culminates in the development of MASH, marked by inflammation and the activation of hepatic stellate cells (HSCs), resulting in fibrosis and eventually progression to irreversible cirrhosis.[4−6] With rarely available medications for MASH and related fibrosis,[7,8] there is an urgent need to develop therapeutic agents with enhanced efficacy.

Received: September 23, 2024
Revised: November 9, 2024
Accepted: November 20, 2024

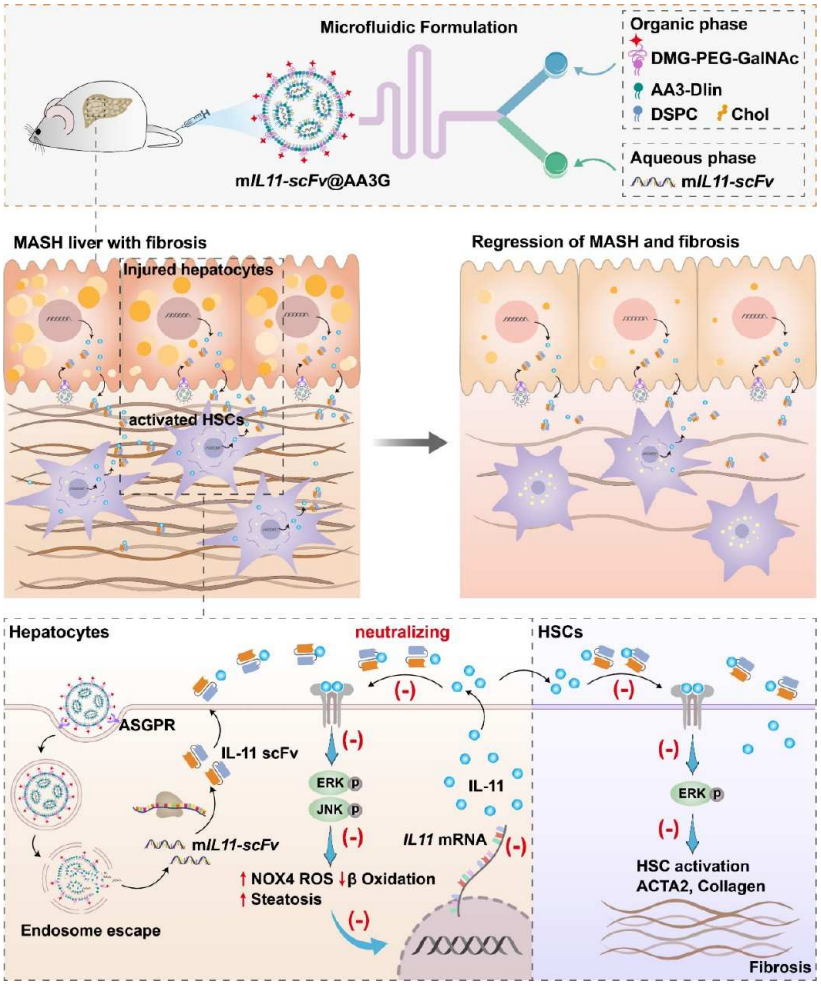

Figure 1. Schematic illustration of m*IL11-scFv*-mediated liver-specific antibody therapy using targeted AA3G LNP for the treatment of MASH and hepatic fibrosis. m*IL11-scFv*@AA3G specifically accumulates in the MASH liver and targets parenchymal hepatocytes through ASGPR-mediated endocytosis. Following internalization, m*IL11-scFv*@AA3G escapes from endosomes and releases therapeutic m*IL11-scFv* into the cytoplasm for IL-11 scFv translation. The secreted IL-11 scFv neutralizes the overexpressed IL-11 in hepatic environments and thereby inhibits the downstream signaling pathway activation in both hepatocytes and HSCs, which results in the regression of MASH and related fibrosis in murine MASH models.

Although the exact mechanism underlying the MASLD-to-MASH transition is complex and multifactorial, hepatocyte lipotoxicity has been considered of central importance.[9−13] Recent studies have confirmed that interleukin-11 (IL-11), secreted by lipid-laden hepatocytes in the lipotoxic milieu, plays a pivotal role in driving the transition from MASLD to MASH.[14,15] In this process, IL-11 exerts autocrine activity by binding to its cognate receptor (IL11ra1) and the glycoprotein 130 (gp130) complex on hepatocytes, then initiating extracellular signal-regulated kinase (ERK) and c-Jun N-terminal kinase (JNK)-dependent signaling pathways, which are responsible for impaired mitochondrial function and reduced fatty acid oxidation, ultimately leading to hepatocyte metabolic dysfunction and cell death. Meanwhile, paracrine IL-11 from lipotoxic hepatocytes activates neighboring HSCs, leading to fibrogenic protein synthesis, extracellular matrix (ECM) deposition, and, eventually, MASH progression.[14,16] We have previously found, in two clinically relevant murine MASH models, that IL-11 expression is significantly upregulated in response to multiple MASH stimuli, which mediates HSC-to-myofibroblast transdifferentiation,[17] thus highlighting the pivotal role of IL-11 in the pathogenesis of MASH. Therefore, developing strategies to specifically deplete overexpressed IL-11 in MASH livers represents an appealing therapeutic approach for the treatment of MASH and hepatic fibrosis.

Antibodies are widely used in cancer, autoimmune, and inflammatory diseases owing to their high affinity and specificity for targeted antigens.[18,19] Despite their effectiveness in treating various diseases, antibody therapies for MASH remain limited primarily due to the lack of organ- or cell-specific targeting as well as unsatisfactory efficacy resulting from their short half-life and instability. Messenger RNA (mRNA) therapeutics have shown significant promise in addressing a variety of diseases and disorders.[20−22] In contrast to traditional protein/antibody drugs, mRNA presents notable advantages such as flexibility, industrial scalability, and the ability to produce any functional protein.[23] With the emergency use authorization of two LNP-based coronavirus disease-2019 (COVID-19) mRNA vaccines, lipid nanoparticles (LNPs) have become the most advanced delivery platform facilitating the clinical translation of mRNA drugs.[24−26] Despite the extensive development of LNP-based mRNA therapeutics for treating various human diseases,[27−29] such as cancers, autoimmune disorders, and infectious diseases, there has been limited exploration of mRNA-mediated liver-

https://doi.org/10.1021/acsnano.4c13404
ACS Nano XXXX, XXX, XXX−XXX

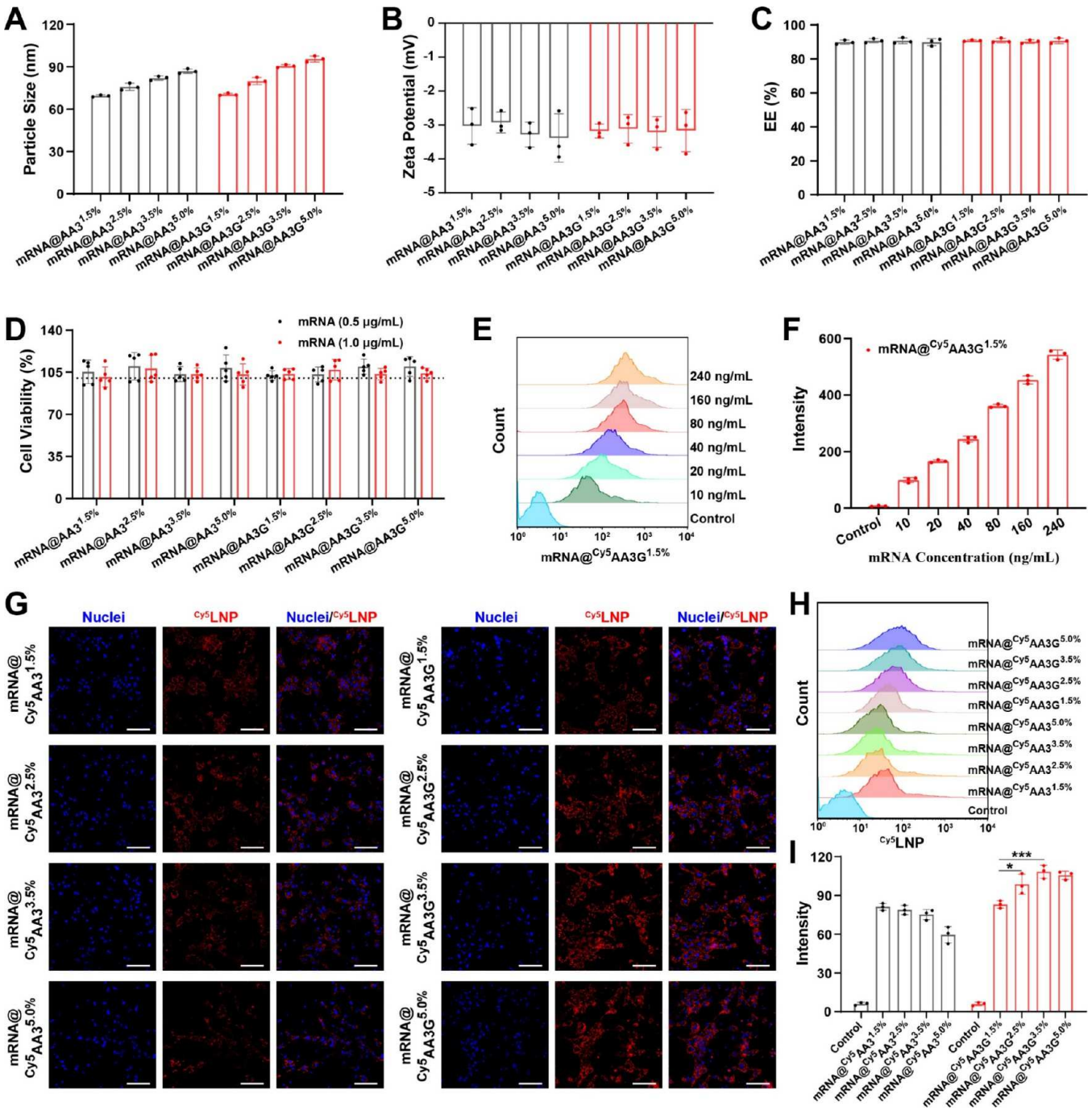

Figure 2. Preparation and characterization of mRNA@AA3G LNP formulations. (A–C) Particle size (A), zeta potential (B), and mRNA encapsulation efficiency (C) of different mRNA-loaded AA3-Dlin LNP formulations (n = 3). (D) Cell viability of primary hepatocytes determined at 48 h post-treatment with various mRNA-loaded AA3-Dlin LNP formulations (n = 5). (E, F) Flow cytometry histogram (E) and mean fluorescence intensity (F) of hepatocytes treated with mRNA@^{Cy5}AA3G$^{1.5\%}$ for 4 h (n = 3). (G–I) Confocal images (G) and flow cytometry analysis (H and I) of hepatocytes treated with indicated LNPs for 4 h (n = 3). Scale bars: 50 μm. Results are presented as means ± SD, and statistical significance was assessed by using one-way ANOVA. *P <0.05, ***P <0.001.

specific antibody therapy for the treatment of MASH and hepatic fibrosis.

Here, we propose delivering IL-11 single-chain variable fragment (scFv)-encoded mRNA (m*IL11-scFv*) to parenchymal hepatocytes, leading to IL-11 scFv antibody expression to neutralize the overexpressed IL-11 in fibrotic hepatic environments and thereby inhibit the pathological IL-11 signaling pathway in both hepatocytes and HSCs (Figure 1). This mRNA-mediated liver-specific antibody therapy was achieved using a targeted LNP delivery platform prepared with an ionizable lipid compound, AA3-Dlin, as we previously reported,[30,31] and N-acetylgalactosamine (GalNAc)-tethered DMG-PEG (DMG-PEG-GalNAc). We further modulated the molar percentages of the GalNAc ligand to identify the optimal LNP formulation (termed m*IL11-scFv*@AA3G) with an enhanced targeting efficiency and mRNA transfection efficacy. In a high-fat- and high-cholesterol (HFHC) diet-induced murine model of early MASH, systemic administration of m*IL11-scFv*@AA3G re-

https://doi.org/10.1021/acsnano.4c13404
ACS Nano XXXX, XXX, XXX−XXX

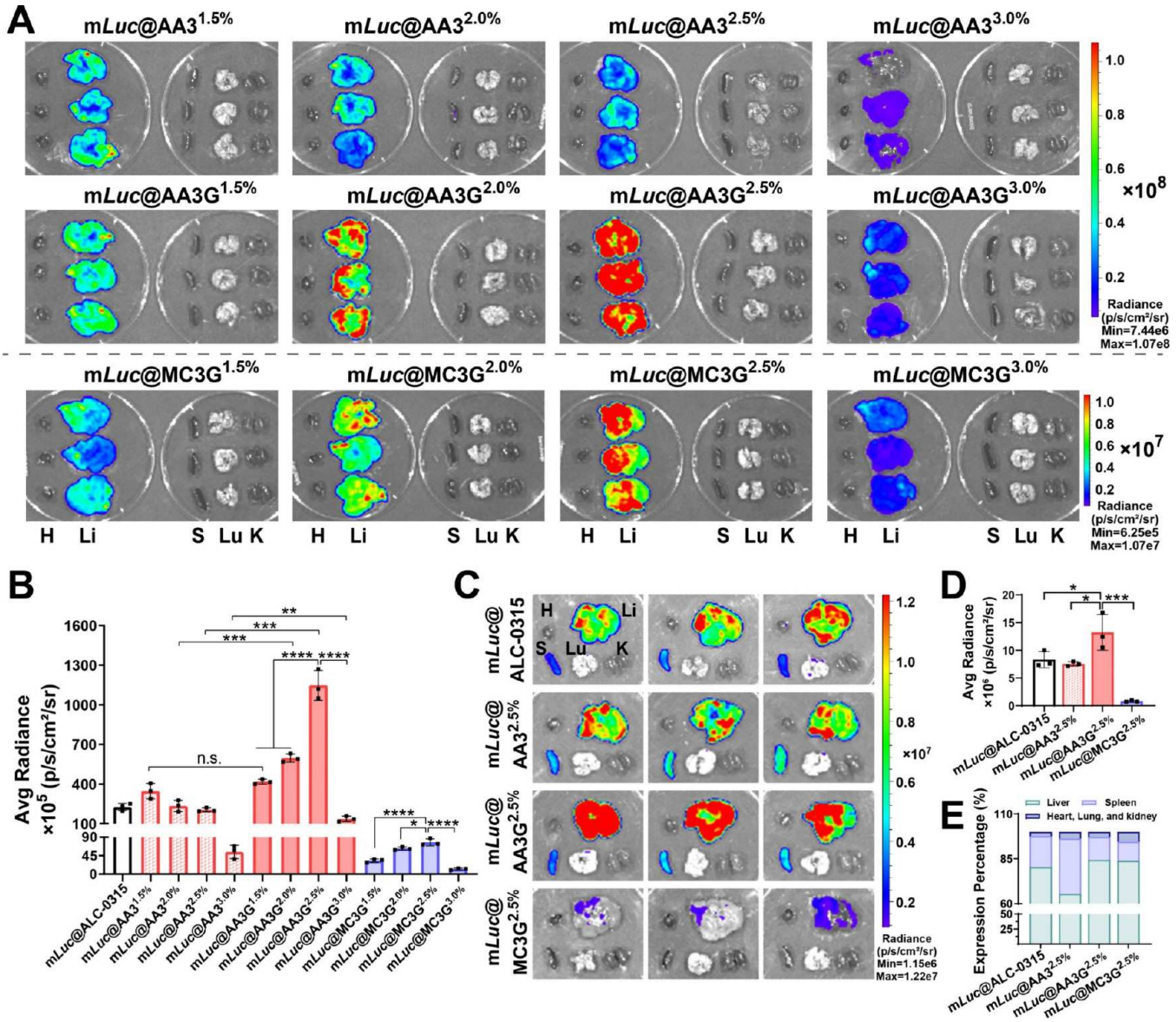

Figure 3. In vivo transfection efficacies of MC3 LNP, AA3 LNP, or ALC-0315 LNP formulations. (A) Ex vivo luminescence imaging of the heart (H), liver (Li), spleen (S), lungs (Lu), and kidneys (K) collected from healthy mice 6 h after treatment with different LNP formulations (n = 3). (B) Quantitative analysis of average radiance in the liver as shown in panel (A) and Figure S5. n = 3. (C) Ex vivo imaging of various organs collected from HFHC diet-induced MASH mice following intravenous injection with the indicated LNPs (n = 3). (D, E) Quantitative analysis of luminescence in the liver (D) and relative luciferase expression percentages in the liver, spleen, and other organs (heart, lungs, and kidneys) (E) as shown in panel (C). n = 3. Results are presented as means ± SD, and statistical significance was assessed using one-way ANOVA and a two-tailed unpaired Student's t-test. *P <0.05, ***P <0.001, ****P <0.0001.

versed MASH and prevented the progression to fibrosis. Notably, mRNA-mediated antibody therapy outperforms IL-11 scFv in reducing steatosis and collagen deposition, as well as restoring liver function, which was attributed to the sustained antibody expression in the liver (up to 9 days) in comparison to IL-11 scFv (~12 h). When administered to mice with established MASH and progressed fibrosis, the targeted m*IL11-scFv*@AA3G nanotherapeutic effectively alleviated steatosis and resolved fibrosis and inflammation. It is worth noting that the targeted AA3G LNP strategy can be applied to other LNP systems such as commercially available Dlin-MC3-DMA (MC3) LNP (the FDA-approved gold standard) since the GalNAc-tethered MC3 LNP exhibits superior transfection efficiency compared to its nontargeted counterpart. Furthermore, our developed AA3G LNP is more efficient than the targeted MC3G LNP and commercial ALC-0315 LNP when compared head-to-head in terms of in vivo delivery efficiency and the therapeutic effect. This work presents a robust targeting LNP platform for mRNA-mediated liver-specific antibody therapy, offering a promising therapeutic approach for treating MASH and hepatic fibrosis, as well as many other diseases.

RESULTS

Synthesis, Characterization, and Optimization of mRNA@AA3G LNP. The targeted mRNA@AA3G LNP formulations were fabricated through self-assembly of a biodegradable ionizable lipid AA3-Dlin, DSPC, cholesterol, and DMG-PEG-GalNAc using a microfluidic method with varying molar ratios (Figure 1). AA3-Dlin was chemically synthesized by enzyme-catalyzed one-step esterification, which

https://doi.org/10.1021/acsnano.4c13404
ACS Nano XXXX, XXX, XXX−XXX

was composed of tertiary amine headgroups originating from piperazine, hydrocarbon chains from unsaturated linolenic acids, and biodegradable ester linkers (Figure S1). Our previous studies have revealed that AA3-Dlin can effectively condense mRNA through electrostatic interaction and facilitate endosomal escape after internalization, resulting in high mRNA translation efficiency in vitro and in vivo.[30] To enhance the hepatic delivery efficiency of LNPs, we synthesized GalNAc-functionalized DMG-PEG as a targeting excipient to specifically bind to the asialoglycoprotein receptor (ASGPR) on parenchymal hepatocytes (Figures S2 and S3). We then fabricated mRNA@AA3G LNP with different molar percentages of DMG-PEG-GalNAc (1.5, 2.5, 3.5, and 5.0%) and assessed their key physicochemical characteristics. mRNA@AA3 LNPs with different molar percentages of DMG-PEG (1.5, 2.5, 3.5, and 5.0%) were formulated in parallel. Figure 2A shows that the particle size of mRNA@AA3G LNP or mRNA@AA3 LNP increased with an increase in the proportion of PEG-lipid and reached a plateau when LNP was formulated with a 5% molar percentage of DMG-PEG-GalNAc (~96 nm) or DMG-PEG (~87 nm) (Figure 2A and Table S1). Additionally, the incorporation of targeting moieties on the surface led to a slight increase in the diameter of mRNA@AA3G LNP compared with its nontargeted counterpart, mRNA@AA3 LNP (Figure 2A and Table S1). Similar results were observed in the MC3 LNP formulations,[32] with an average diameter of 102 nm in the mRNA@MC3G$^{5\%}$ group and 95 nm in the mRNA@MC3$^{5\%}$ group (Figure S4 and Table S1). All mRNA@AA3G LNP and mRNA@AA3 LNP formulations showed a nearly neutral zeta potential (approximately −3 mV) and an mRNA encapsulation efficiency (EE) of around 90% (Figure 2B,C). In vitro cytotoxicity was assessed in mouse primary hepatocytes using a cell counting kit-8 (CCK8) assay. As shown in Figure 2D, none of the LNPs exhibited noticeable cytotoxicity after 48 h of treatment, even at a high mRNA concentration of 1.0 μg/mL.

To evaluate cellular internalization in vitro, mRNA@AA3G LNP incorporated with a 1.5% molar percentage of DMG-PEG-GalNAc was formulated using Cy5-labeled cholesterol to yield a Cy5-labeled LNP (mRNA@^{Cy5}AA3G$^{1.5\%}$). The resultant mRNA@^{Cy5}AA3G$^{1.5\%}$ was incubated with primary hepatocytes at varying mRNA concentrations for 4 h and then analyzed by flow cytometry. The results revealed a dose-dependent internalization of mRNA@^{Cy5}AA3G$^{1.5\%}$ by hepatocytes (Figure 2E,F). We then used an mRNA concentration of 40 ng/mL to explore the impact of the DMG-PEG-GalNAc incorporation percentage on the cellular uptake in primary hepatocytes. As depicted in Figure 2G−I, cells treated with targeted mRNA@^{Cy5}AA3G LNP displayed a higher Cy5 signal intensity compared to those treated with its nontargeted counterpart mRNA@^{Cy5}AA3 LNP. Furthermore, increasing the proportion of DMG-PEG-GalNAc enhanced the endocytosis of mRNA@^{Cy5}AA3G LNP by hepatocytes, reaching a plateau at a 3.5% molar percentage of targeting moiety incorporation. These results suggest that the incorporation of the GalNAc moiety enhances the internalization of AA3-Dlin LNP in primary hepatocytes.

In Vivo mRNA Delivery of mRNA@AA3G LNP. To evaluate the in vivo transfection efficiency of the mRNA@AA3G LNP formulations, luciferase-encoding mRNA (m*Luc*) was encapsulated into mRNA@AA3G or mRNA@AA3 to formulate m*Luc*@AA3G or m*Luc*@AA3. The fabricated LNPs were intravenously administered into healthy C57BL/6J mice at a dose of 3 μg of m*Luc* per mouse, and the luminescence intensity was analyzed after 6 h. Commercially available MC3 and ALC-0315 LNP formulations were used as positive controls, with their physicochemical parameters listed in Table S1. Consistent with the cellular uptake results, all m*Luc*@AA3G LNP groups demonstrated higher luciferase expression in the liver compared to their nontargeted m*Luc*@AA3 LNP counterparts as shown in Figure 3A,B, indicating that incorporation of GalNAc moiety increased the mRNA delivery efficiency in the liver. The liver-specific luciferase expression increased as the incorporated GalNAc moiety increased to or below a molar percentage of 2.5%, whereas continuously increasing the GalNAc moiety to 3.0% sharply decreased the luminescence intensity. m*Luc*@AA3G$^{2.5\%}$ resulted in the highest luciferase bioluminescence intensity in the liver among all of the LNPs tested (Figure 3A,B and Figure S5). Interestingly, the liver luciferase expression decreased as the molar ratio of incorporated DMG-PEG increased, probably ascribed to the increased steric hindrance of PEG chains that hinder cellular internalization and endosomal escape.[33,34] This targeting strategy can also be applied to the commercially available MC3 LNP.[32] Similarly, the incorporation of GalNAc moiety increased liver-specific mRNA transfection efficiency of MC3 LNPs compared to their nontargeted counterparts, with MC3G LNP prepared using DMG-PEG-GalNAc at a 2.5% molar percentage demonstrating the highest liver luciferase expression (Figure 3A and Figure S6). Notably, m*Luc*@AA3G$^{2.5\%}$ resulted in a 5.6-fold higher bioluminescence intensity in the liver compared to m*Luc*@AA3$^{2.5\%}$, and 5.1- and 14.7-fold higher than m*Luc*@ALC-0315 and m*Luc*@MC3G$^{2.5\%}$, respectively (Figure 3B).

The mRNA delivery efficacy of the above-mentioned LNPs was further examined in the HFHC diet-induced murine MASH model with progression fibrosis. HFHC mice receiving m*Luc*@AA3G$^{2.5\%}$ treatment demonstrated the highest liver-specific bioluminescence intensity, showing a 1.8-, 1.6-, and 16.1-fold increase compared to m*Luc*@AA3$^{2.5\%}$, m*Luc*@ALC-0315, and m*Luc*@MC3G$^{2.5\%}$, respectively (Figure 3C,D). Among the imaged tissues, 84.4% of the total luciferase came from the liver in AA3G$^{2.5\%}$ LNP-treated mice, compared to 65.5% in AA3$^{2.5\%}$ LNP-treated mice (Figure 3E). We also investigated the biodistribution of Cy5-labeled m*IL11-scFv*@^{Cy5}AA3 and m*IL11-scFv*@^{Cy5}AA3G in the fibrotic MASH models. Consistent with the enhanced liver expression of AA3G LNP shown in Figure 3C−E, ^{Cy5}AA3G LNP exhibited a higher and more specific distribution in the liver compared to the nontargeted ^{Cy5}AA3 LNP (Figure S7). Quantification of the Cy5 fluorescence intensity indicated an approximately 1.5-fold increase in the accumulation of ^{Cy5}AA3G LNP in the liver compared to ^{Cy5}AA3 LNP, with 63.6 and 50.8% of the total fluorescence being observed in the liver of ^{Cy5}AA3G LNP- and ^{Cy5}AA3 LNP-treated mice, respectively (Figure S7B,C). As a result, mRNA@AA3G LNP with 2.5% DMG-PEG-GalNAc was used in the following studies.

To determine the specific cell subtypes transfected by the ^{Cy5}AA3G LNP, we further digested liver tissues and harvested primary hepatocytes and nonparenchymal cells for flow cytometry analysis (Figure S8). As shown in Figure S9, ^{Cy5}AA3G LNP transfected 78.2% of hepatocytes in the liver, which was 1.5-fold higher than that of the nontargeted ^{Cy5}AA3 LNP (53.5%). Both LNPs, however, exhibited similar transfection efficiencies in endothelial cells (~80%), Kupffer cells (~75%), and HSCs (~24%). These results align with the in vitro data (Figure 2G−I) and demonstrate that m*IL11-scFv*@AA3G

https://doi.org/10.1021/acsnano.4c13404
ACS Nano XXXX, XXX, XXX−XXX

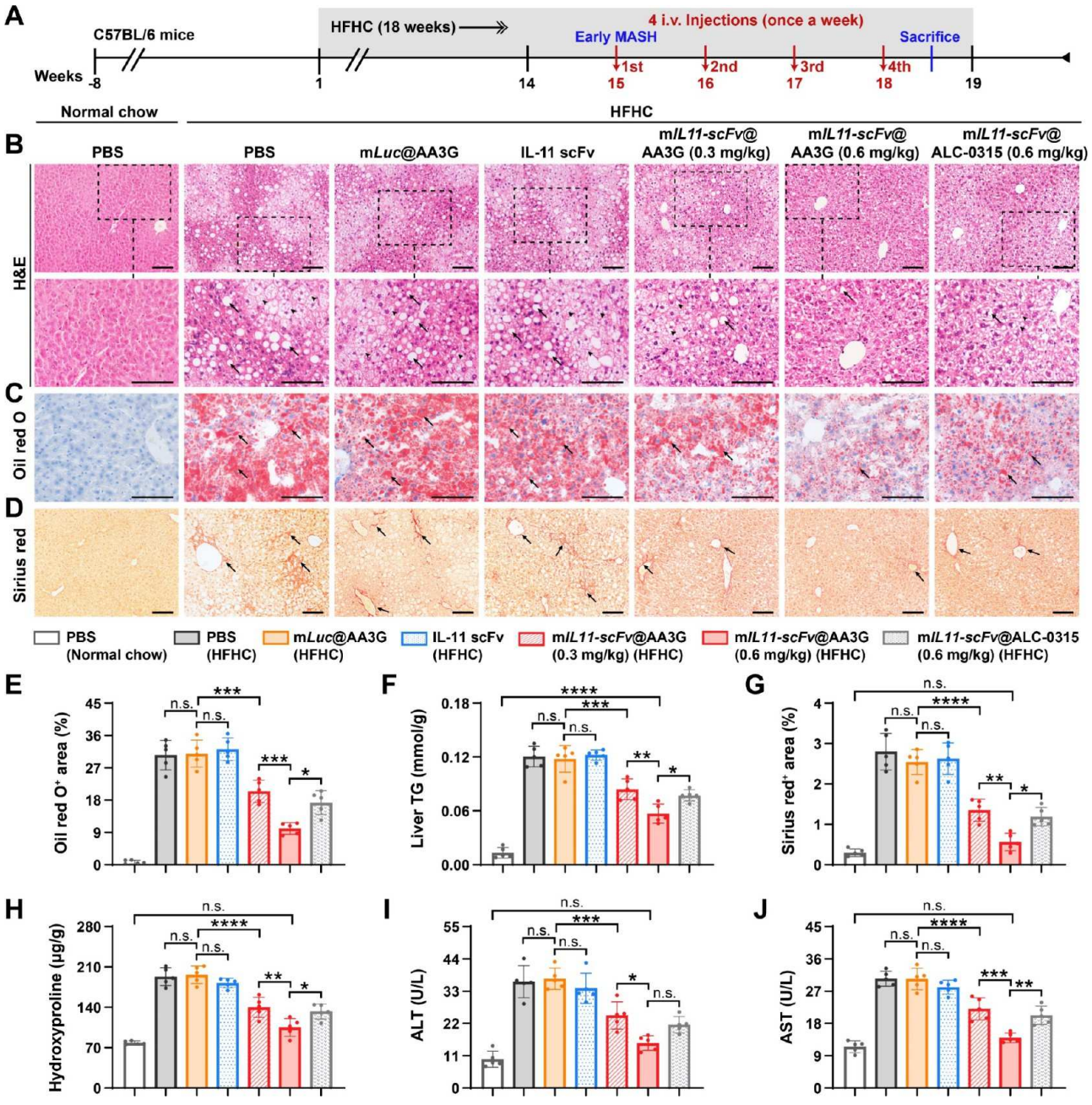

Figure 4. AA3G LNP-mediated hepatic expression of IL-11 scFv reverses MASH and prevents MASH progression to fibrosis. (A) Schematic diagram of the experimental design. Mice were fed with the HFHC diet for a total of 18 weeks. At week 15, mice were intravenously injected with indicated treatments once weekly for 4 weeks. Samples were harvested 4 days after the final injection. (B–D) H&E staining (the black arrows and black arrowheads indicate macro- and microvesicular steatosis, respectively) (B), Oil red O staining (lipid droplets are stained red and indicated by black arrows) (C), and Sirius red staining (collagen I and III fibers are stained red and indicated by black arrows) (D) of liver tissues collected from healthy mice or HFHC diet-fed mice receiving indicated treatments. Scale bars, 100 μm. (E) Quantitative analysis of Oil red O-positive area in liver sections (n = 5). (F) Liver triglyceride content (n = 5). (G) Quantitative analysis of Sirius red-positive area in liver sections (n = 5). (H) Measurement of the hydroxyproline concentration in liver homogenates (n = 5). (I, J) Serum ALT (I) and AST (J) levels (n = 5). Results are presented as means ± SD, and statistical significance was assessed using one-way ANOVA. *P <0.05, **P <0.01, ***P <0.001, ****P <0.0001, n.s., not significant, P > 0.05.

significantly increases the level of LNP internalization in hepatocytes in vivo.

Pharmacokinetics and Antibody Expression of m*IL11-scFv*@AA3G. We encapsulated *IL-11 scFv* mRNA (m*IL11-scFv*) into the targeted AA3-Dlin LNP to formulate m*IL11-scFv*@AA3G. As shown in Figure S10, m*IL11-scFv*@AA3G displayed a spherical structure under transmission electron microscopy (TEM), with an average particle size of 81.3 nm and a polydispersity index (PDI) of 0.132. The m*IL11-scFv* encapsulated within AA3G LNP demonstrated good stability when incubated with 10% fetal bovine serum (FBS) for up to 48 h, whereas it rapidly degraded in its naked form (Figure S11A). Stability was further assessed by monitoring the particle size and turbidity at 37 °C in the presence of serum to simulate physiological conditions. As shown in Figure S11B,C, there were no significant changes in particle size or serum-induced

https://doi.org/10.1021/acsnano.4c13404
ACS Nano XXXX, XXX, XXX−XXX

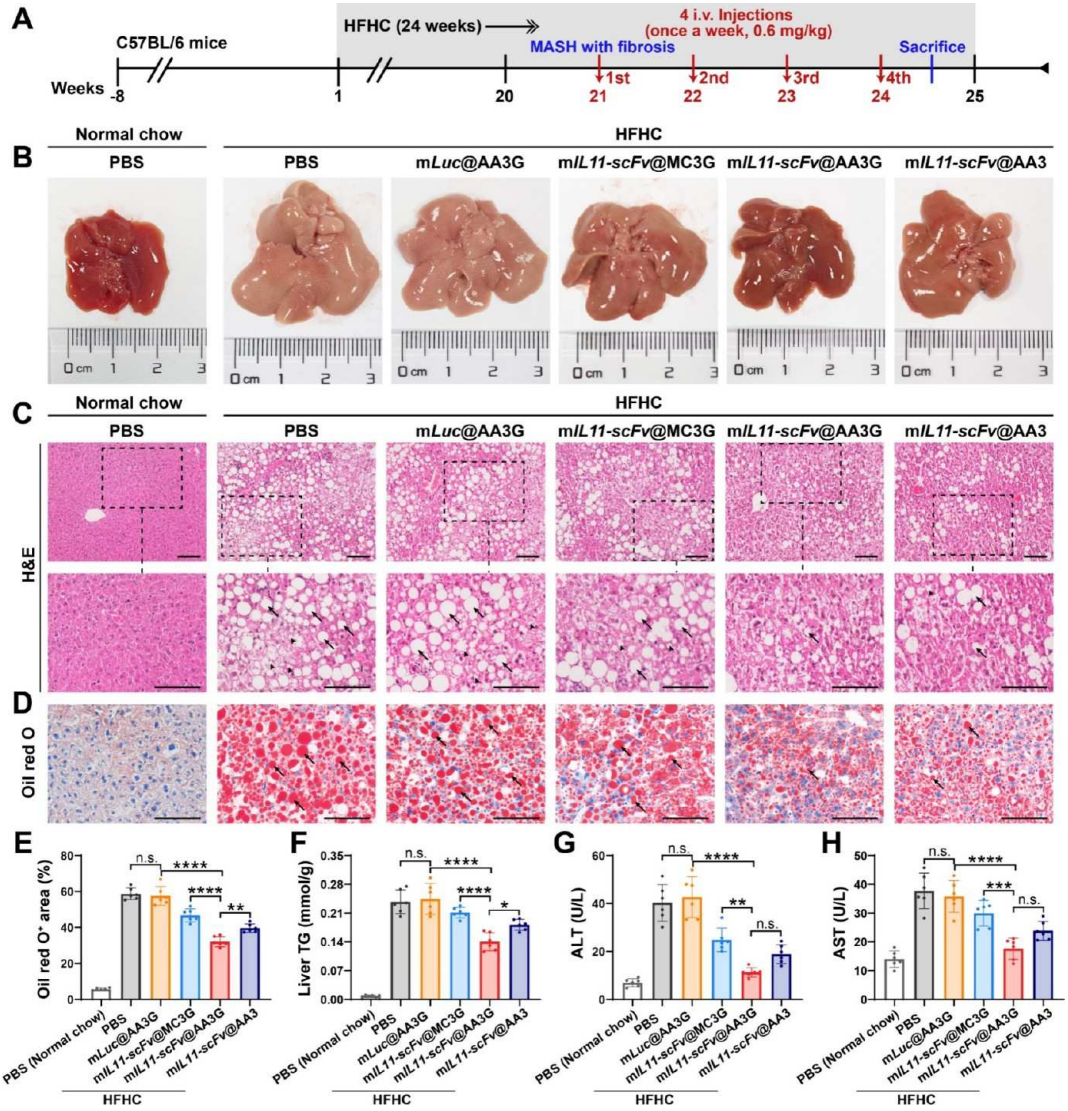

Figure 5. m*IL11-scFv*@AA3G treatment ameliorates steatosis and liver damage in established MASH with fibrosis. (A) Schematic diagram illustrates the establishment of a MASH model with fibrosis and the treatment regimen. Mice were fed with an HFHC diet for a total of 24 weeks. At week 21, mice were intravenously injected with the indicated treatments once weekly for an additional 4 weeks and sacrificed 4 days after the final injection for analysis. (B) Representative gross morphology of livers collected from healthy mice or HFHC diet-fed mice treated with PBS, m*Luc*@AA3G, m*IL11-scFv*@MC3G, m*IL11-scFv*@AA3G, or m*IL11-scFv*@AA3. (C, D) Representative images of liver tissue sections stained with H&E (black arrows and black arrowheads indicate macro- and microvesicular steatosis, respectively) (C) or Oil Red O (lipid droplets are red and indicated by black arrows) (D). Scale bars, 100 μm. (E) Quantitative analysis of Oil red O-positive area in liver sections (n = 5). (F) Liver triglyceride content (n = 5). (G) Serum ALT levels (n = 5). (H) Serum AST levels (n = 5). Results are presented as means ± SD, and statistical significance was assessed using one-way ANOVA. *P < 0.05, **P < 0.01, ***P < 0.001, ****P < 0.0001, n.s., not significant, P > 0.05.

aggregation of m*IL11-scFv*@AA3G over the 48 h period. These results suggest that the AA3G LNP formulation provides a stable nanostructure capable of protecting encapsulated mRNA from degradation.

The pharmacokinetics and expression duration of Cy5-labeled m*IL11-scFv*@^{Cy5}AA3G were then investigated in an HFHC diet-induced MASH model with fibrosis, using both a high dose (0.6 mg/kg of m*IL11-scFv*) and a low dose (0.3 mg/kg of m*IL11-scFv*). Blood levels of ^{Cy5}AA3G rapidly increased within 12 h, peaked at 24 h, and decreased to a weakly detectable level 8 days postinjection, demonstrating a dose-dependent response (Figure S12). We also measured hepatic levels of IL-11 scFv using an enzyme-linked immunosorbent assay (ELISA) at designated time points following intravenous administration. m*IL11-scFv*@AA3G demonstrated a dose-dependent, sustained expression of scFv antibody in the liver, as illustrated in Figure S13. The hepatic levels of IL-11 scFv, translated endogenously by m*IL11-scFv*@AA3G, peaked within 3 days postadministration and sustained for up to 9 days. In contrast, hepatic antibody levels showed a transient increase within 1 h following administration of free IL-11 scFv, but these levels rapidly decreased within 6 h, dropping to barely detectable levels after 12 h due to the short half-life of IL-11 scFv (Figure S13). The lag between LNP retention time and expression duration is likely due to the half-life of m*IL11-scFv*, the expression kinetics of m*IL11-scFv*-LNP, and the stability of expressed antibody in the liver.[35,36] Based on the findings, we selected a weekly dosing interval to minimize the frequency of administration in subsequent experiments.

https://doi.org/10.1021/acsnano.4c13404
ACS Nano XXXX, XXX, XXX−XXX

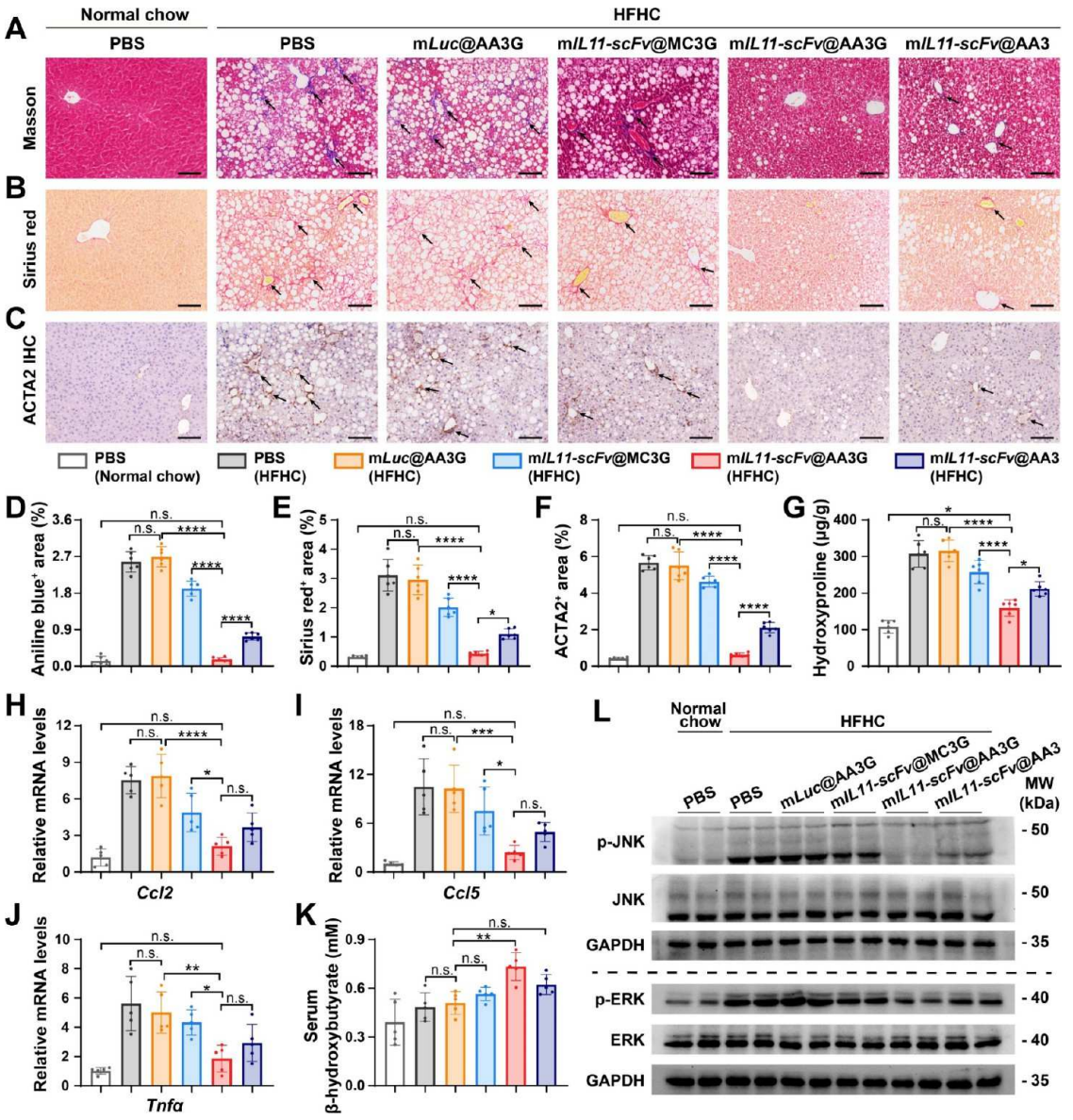

Figure 6. m*IL11-scFv*@AA3G treatment resolves fibrosis and inflammation via inhibiting the IL-11 signaling pathway in established MASH with fibrosis. (A, B) Representative images of liver tissue sections stained with Masson's trichrome (collagen fibers are stained blue and indicated by black arrows) (A) or Sirius red (collagen I and III fibers are stained red and indicated by black arrows) (B). Scale bars: 100 μm. (C) Immunohistochemistry staining of ACTA2 in liver tissues. Scale bars, 100 μm. (D−F) Quantitative analysis of aniline blue-positive area (D), Sirius red-positive area (E), and ACTA2-positive area (F) in liver tissue sections ($n = 5$). (G) Measurement of the hydroxyproline concentration in liver homogenates ($n = 5$). (H−J) Relative mRNA expression levels of proinflammation genes *Ccl2* (H), *Ccl5* (I), and *Tnfα* (J) in the livers of mice after various treatments ($n = 5$). (K) Serum β-hydroxybutyrate levels ($n = 5$). (L) Western blots of p-JNK and p-ERK expression in liver homogenates. Results are presented as means ± SD, and statistical significance was assessed using one-way ANOVA. *P <0.05, **P <0.01, ***P <0.001, ****P <0.0001, n.s., not significant, $P > 0.05$.

m*IL11-scFv*@AA3G Reverses MASH and Prevents the Progression to Fibrosis in an Early MASH Model. We next examined whether m*IL11-scFv*@AA3G could prevent MASH progression to fibrosis in a murine model of early MASH with no obvious features of fibrosis (on HFHC diets for 14 weeks), where treatment began after steatosis and inflammation had been established and continued as the disease progressed to fibrosis (on HFHC diets for 18 weeks). C57BL/6J mice were fed with an HFHC diet for a total of 18 weeks to develop MASH with fibrosis. Starting at week 15, the mice received weekly intravenous injections of m*Luc*@AA3G, m*IL11-scFv*@ALC-0315, or m*IL11-scFv*@AA3G at either a high or low dose for 4 weeks, with PBS-treated groups serving as negative controls (Figure 4A). Additionally, a separate control group was administered purified IL-11 scFv antibody at a typical dosage of 10 mg/kg to achieve therapeutic concentrations.[16,37] On the fourth day after the last administration at week 18, we sacrificed mice and conducted histological analysis to assess hallmarks associated with steatosis and fibrosis in the liver tissues. As shown in Figure 4B,C,E, HFHC diet feeding induced significant macro- and microvesicular lipid droplets, as shown by representative hematoxylin and eosin (H&E) and Oil red O staining of liver sections from PBS, m*Luc*@AA3G, or IL-11 scFv antibody control group. Both AA3G- and ALC-0315-formulated m*IL11-scFv* nanotherapeutics markedly ameliorated steatosis and reduced Oil red O-stained lipid deposition in liver tissues,

https://doi.org/10.1021/acsnano.4c13404
ACS Nano XXXX, XXX, XXX−XXX

with the high dose of m*IL11-scFv*@AA3G treatment exhibiting a more pronounced effect compared to m*IL11-scFv*@ALC-0315 or the low dose of m*IL11-scFv*@AA3G treatment (Figure 4B,C,E). These results were further supported by a reduction in hepatic steatosis, as measured by the total liver triglyceride (TG) content in HFHC mice (Figure 4F).

Sirius red staining demonstrated that the fibrotic regions were markedly increased in the livers of HFHC mice treated with PBS, m*Luc*@AA3G, or IL-11 scFv antibody compared to those of normal chow-fed healthy mice (Figure 4D,G). All m*IL11-scFv* treatments reduced the number of Sirius red-positive areas in liver tissues. Notably, HFHC mice receiving the high dose of m*IL11-scFv*@AA3G effectively prevented MASH progression to fibrosis, as evidenced by the barely detectable regions comparable to healthy mice. Hydroxyproline constitutes approximately 14% of the total amino and imino acids in fibrillar collagen, serving as a key indicator of fibrosis severity when assessed based on tissue concentration.[38,39] Consistent with the Sirius red staining results, the liver hydroxyproline content was substantially decreased by m*IL11-scFv*@AA3G and m*IL11-scFv*@ALC-0315 treatments, especially at the 0.6 mg/kg dose of m*IL11-scFv*@AA3G, confirming the successful prevention of fibrosis development (Figure 4H).

We observed significantly increased levels of serum ALT and AST, the liver damage biomarkers in HFHC mice receiving PBS, m*Luc*@AA3G, or IL-11 scFv antibody treatment when compared to healthy controls (Figure 4I,J). Intriguingly, the HFHC diet-induced elevation in serum ALT and AST was nearly restored to normal levels following intervention with a high dose of m*IL11-scFv*@AA3G, indicating a recovery in liver function (Figure 4I,J). Taken together, these results suggest that m*IL11-scFv*@AA3G-mediated liver-specific antibody therapy reverses MASH and halts the progression to hepatic fibrosis in an established murine MASH model, demonstrating superior therapeutic efficacy compared to the commercial ALC-0315 formulation and scFv antibody therapy.

m*IL11-scFv*@AA3G Ameliorates Hepatic Steatosis and Resolves Fibrosis and Inflammation in the Established MASH Model with Fibrosis. Progressive fibrosis is the main predictor of liver-related mortality and overall survival in MASH,[40,41] and the primary end point for MASH therapies has been shifting toward ameliorating fibrosis without worsening of MASH.[42] For these reasons, the therapeutic effects of m*IL11-scfv*@AA3G were further verified in a well-established MASH model with progressive fibrosis induced by HFHC diets. C57BL/6J mice were fed with an HFHC diet for 20 weeks to develop pronounced steatosis, ballooning, inflammation, and fibrosis. At week 21, mice were injected with different formulations via tail vein once a week for 4 weeks and sacrificed on the fourth day after the last injection (Figure 5A). HFHC mice treated with PBS or m*Luc*@AA3G displayed enlarged liver volume, significant macro- and microvesicular steatosis, increased lipid accumulation, and liver TG content as evidenced by morphological images, H&E staining, Oil red O staining, and quantitative analysis of liver TG (Figure 5B−F). All these symptoms were alleviated in mice receiving m*IL11-scFv* nanotherapeutics, with the targeted AA3G LNP-formulated mRNA therapy demonstrating a superior effect compared to either the nontargeted AA3 LNP or the targeted benchmark MC3G LNP. Serological analysis showed that liver damage biomarkers, ALT and AST, in the group treated with m*IL11-scFv*@AA3G, were nearly restored to normal levels, suggesting liver function recovery (Figure 5G,H).

Masson and Sirius red staining showed a substantial increase in collagen deposition within the liver tissues of HFHC mice receiving PBS or m*Luc*@AA3G treatment (Figure 6A,B,D,E). m*IL11-scFv*@AA3G treatment successfully restored established hepatic fibrotic morphology to a nearly normal liver architecture, while both m*IL11-scFv*@MC3G and m*IL11-scFv*@AA3 demonstrated a comparatively weaker antifibrotic effect (Figure 6A,B,D,E). In parallel, immunohistochemistry staining revealed an almost negligible ACTA2-positive area in the liver sections from the mice receiving m*IL11-scFv*@AA3G, indicating a diminished level of activation of HSCs and an effective resolution of fibrosis (Figure 6C−F). Consistent with the histological results, we also observed the lowest level of hepatic hydroxyproline following m*IL11-scFv*@AA3G treatment, decreasing from 316 μg/g (m*Luc*@AA3G) to 159 μg/g in wet liver tissues (Figure 6G).

Quantitative real-time polymerase chain reaction (qRT-PCR) was also conducted to analyze the expression of proinflammatory chemokines involved in MASH progression, including tumor necrosis factor alpha (*Tnfα*) and C−C motif chemokine ligands 2 (*Ccl2*) and *Ccl5*. HFHC mice receiving PBS or m*Luc*@AA3G exhibited significantly increased expression of *Tnfα*, *Ccl2*, and *Ccl5* in the liver homogenates as shown in Figure 6H−J, but a notable reduction in the expression levels of the aforementioned proinflammatory genes was observed in animals receiving m*IL11-scFv* (Figure 6H−J). It is worth noting that treatment with m*IL11-scFv*@AA3G exhibited the most potent inhibition of proinflammatory gene production in the liver, nearly restoring *Tnfα*, *Ccl2*, and *Ccl5* levels to normal ranges of healthy controls (Figure 6H−J). The infiltrating hepatic inflammatory cells in fibrotic MASH mice were also analyzed by flow cytometry (Figure S14). As shown in Figure S15, HFHC diet-fed mice exhibited pronounced hepatitis, with a significantly increased percentage of liver-infiltrating $CD8^+$ T cells, proinflammatory monocytes, and monocyte-derived macrophages (MoMFs) compared to healthy controls. Both m*IL11-scFv*@AA3 and m*IL11-scFv*@AA3G nanotherapeutics decreased the level of inflammatory cell infiltration in the liver. Notably, the targeted m*IL11-scFv*@AA3G treatment reduced $CD8^+$ T cells, proinflammatory monocytes, and MoMFs to near-normal levels.

To investigate the underlying mechanisms for m*IL11-scFv*-mediated amelioration of MASH and hepatic fibrosis, we evaluated the serum levels of β-hydroxybutyrate, a peripheral marker indicating liver fatty acid oxidation. As shown in Figure 6K, only m*IL11-scFv*@AA3G-treated mice exhibited markedly increased serum levels of β-hydroxybutyrate among groups, suggesting that the targeted AA3G LNP-mediated hepatic expression of IL-11 scFv reduces steatosis by promoting fatty acid oxidation in lipid-loaded hepatocytes. Quantitative analysis of liver homogenates showed that IL-11 upregulation observed in HFHC mice was inhibited following m*IL11-scFv*-mediated antibody therapy, with m*IL11-scFv*@AA3G demonstrating the lowest expression levels of IL-11 (Figure S16). The phosphorylation of JNK and ERK induced by IL-11 is thought to be associated with hepatocyte metabolic dysfunction and HSC activation during MASH progression. Western blotting results showed that m*IL11-scFv*@AA3G treatment most effectively inhibited pathological JNK and ERK activation in the livers of HFHC mice among the groups (Figure 6L, Figure S17, and Table S2). These results indicate that liver-specific antibody therapy mediated by m*IL11-scFv*@AA3G effectively ameliorates steatosis as well as resolves fibrosis and inflammation in a murine MASH model with established fibrosis. The therapeutic efficacy

https://doi.org/10.1021/acsnano.4c13404
ACS Nano XXXX, XXX, XXX−XXX

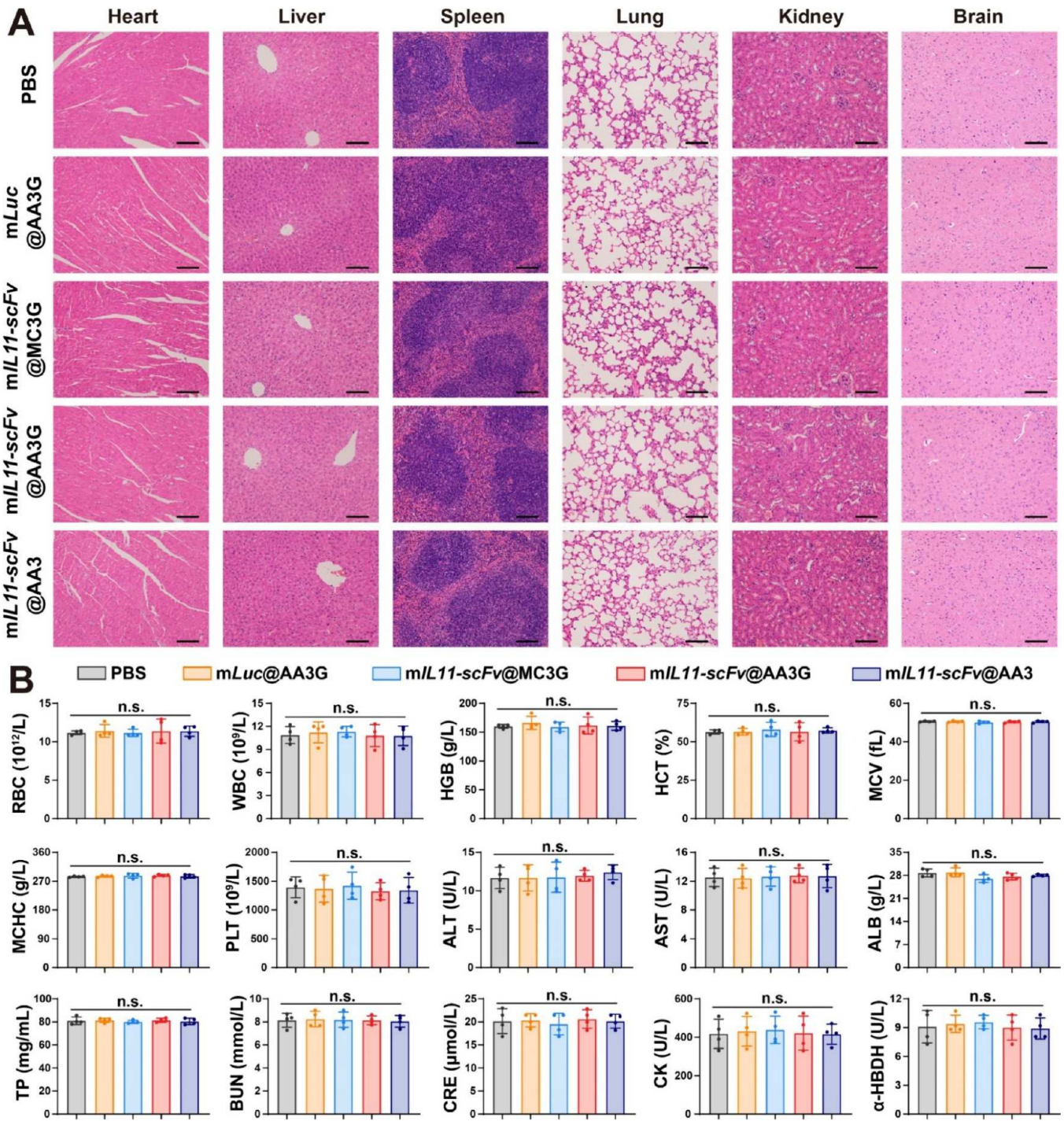

Figure 7. In vivo safety profiles. (A) Pathological analyses of the heart, liver, spleen, lung, kidney, and brain in healthy mice 4 days after the last injection of various treatments. Scale bars, 100 μm. (B) Hematological and biochemical analyses in healthy mice following the indicated treatments (n = 4). The tested parameters include the peripheral blood cells (RBC, WBC, HGB, HCT, MCV, MCHC, and PLT), liver functions (ALT, AST, ALB, and TP), renal functions (BUN and CRE), and heart functions (CK and α-HBDH). Results are presented as means ± SD, and statistical significance was assessed using one-way ANOVA. n.s., not significant, $P > 0.05$.

of this approach is achieved through inhibition of the IL-11 signaling pathway.

In Vivo Safety Evaluation. The in vivo biosafety studies of m*IL11-scfv*@AA3G was evaluated in healthy C57BL/6J mice. Briefly, mice were randomly allocated into five groups and intravenously administered with PBS, m*Luc*@AA3G, m*IL11-scFv*@MC3G, m*IL11-scFv*@AA3, or m*IL11-scFv*@AA3G once a week for 4 weeks. The mice were anesthetized and sacrificed 4 days after the last treatment. Blood was obtained from the retro-orbital sinus for the analysis of biochemical and hematological parameters, while major organs such as the brain, heart, liver, spleen, lung, and kidney were collected for H&E staining. As shown in Figure 7A, mice receiving m*Luc* or m*IL11-scFv* therapeutics showed no obvious pathological abnormalities, degenerations, or lesions compared to healthy controls. Hematological parameters, including red blood cells (RBC),

https://doi.org/10.1021/acsnano.4c13404
ACS Nano XXXX, XXX, XXX−XXX

white blood cells (WBC), hemoglobin (HGB), hematocrit (HCT), mean corpuscular volume (MCV), mean corpuscular hemoglobin concentration (MCHC), and platelets (PLT), remained within the normal range in all groups (Figure 7B). This suggests that the administered mRNA therapeutics did not induce an acute infection or hemolytic anemia throughout the treatment period. Biochemical analysis revealed that m*Luc* or m*IL11-scFv* therapy did not cause any significant changes in liver functions (ALT, AST, albumin (ALB), and total protein (TP)), renal functions (blood urea nitrogen (BUN) and serum creatinine (CRE)), and heart functions (creatine kinase (CK) and α-hydroxybutyrate dehydrogenase (α-HBDH)) when compared to healthy controls, suggesting negligible hepatotoxicity, nephrotoxicity, and cardiotoxicity of LNP-mRNA nanotherapeutics (Figure 7B). The possible side effects of mRNA-LNPs were also evaluated in the above-mentioned fibrotic MASH model after the last administration. H&E staining revealed no apparent injuries in the heart, spleen, lung, or kidney tissues across all treated groups (Figure S18). Combined with the safety profile assessed in healthy mice (Figure 7), these results suggest that intravenous administration of m*IL11-scFv* nanotherapeutics is relatively safe at the tested dosage.

DISCUSSION

MASH is a complex metabolic syndrome characterized by excessive liver fat accumulation and chronic inflammation, typically accompanied by progressive fibrosis.[4,6] Various pharmaceutical interventions have been developed with the aim of resolving MASH features and reducing fibrosis. These therapies include targets involved in metabolism (e.g., glucose, cholesterol, and lipid metabolism), cellular stress, inflammation cascades, and fibrosis.[43,44] Despite extensive investigation, MASH drug development remains challenging due to the lack of liver-specific and effective therapeutic drugs. There is a critical need to develop strategies with enhanced specificity and therapeutic efficacy to meet the increasing clinical demand for MASH.

IL-11 is a vital cytokine that is overexpressed by lipotoxic hepatocytes and activated HSCs in the MASH liver, driving the MASLD-to-MASH transition and fibrosis progression. Our previous study has shown that IL-11 expression is significantly upregulated and mediates HSC-to-myofibroblast transformation in two clinically relevant murine MASH models, revealing the crucial role of IL-11 in MASH pathogenesis. Herein, we hypothesize that specifically neutralizing excess secreted IL-11 in fibrotic liver environments may be an effective strategy to reverse MASH and related fibrosis. Full-length antibodies hold great therapeutic potential due to their exceptional specificity and high antigen affinity. However, scFvs offer several distinct advantages, including smaller molecular weight, enhanced permeability, lower immunogenicity, and flexible modular design, making them more suitable for chronic conditions like MASH, which typically require efficient penetration into fibrotic livers and long-term treatment.[45,46] Despite these benefits, the short half-life of scFvs limits their application. In this work, we designed liver-specific antibody therapy by leveraging advances in the mRNA technology. Our approach involved developing a liver-targeting LNP loaded with m*IL11-scFv* to realize sustained IL-11 scFv antibody expression in hepatic lesions. Compared to siRNA therapeutics targeting the IL-11 signaling pathway, which theoretically silence only target genes in transfected cells but typically require extensive sequence screening and backbone modification optimization during research and development,[47,48] m*IL11-scFv*-mediated antibody therapy offers the advantages of neutralizing overexpressed IL-11 across entire fibrotic lesions, potentially reducing the off-target effects associated with siRNA therapy while avoiding the risk of suppressing essential IL-11 production in the liver. The developed LNP comprises: (1) a self-made ionizable lipid, (2) DSPC and Chol, and (3) lipid-PEG or lipid-PEG-GalNAc conjugate where GalNAc was utilized to realize the targeting design. We synthesized GalNAc-tethered DMG-PEG to enhance the mRNA delivery efficiency to hepatic lesions due to the strong affinity between GalNAc and ASGPR on parenchymal hepatocytes.[49,50] The liver-targeting LNP formulation was determined by screening the hepatic transfection efficiency of AA3-Dlin LNPs incorporated with varying molar percentages of DMG-PEG-GalNAc. In vivo results revealed that AA3-Dlin LNP incorporating 2.5% DMG-PEG-GalNAc yielded the highest level of luciferase expression in the liver, accounting for 84.4% of the bioluminescence among all tissues. Additionally, this targeting strategy can also be applied to commercially available MC3 LNP since the GalNAc-tethered MC3 LNP results in superior transfection efficiency compared to its original counterpart. Notably, our developed AA3G LNP is more efficient than the targeted MC3G LNP and commercial ALC-0315 LNP in terms of in vivo delivery efficiency and the therapeutic effect. The concentration and duration of antibody expression in the liver are determined by the half-life of the mRNA, the expression kinetics of mRNA-LNP, and the stability of the expressed antibody.[35,36] In an HFHC diet-induced MASH model, systemic administration of 0.6 mg/kg of the m*IL11-scFv*@AA3G resulted in prolonged IL-11 scFv antibody persistence in the liver for up to 9 days, whereas IL-11 scFv levels were barely detectable 12 h after injection of 10 mg/kg of IL11-scFv antibody alone.

The administration dose and efficacy evaluation were initially investigated in an HFHC diet-induced early MASH model. Histological and serological analyses showed that both 0.3 and 0.6 mg/kg of m*IL11-scFv*@AA3G treatments mitigated steatosis, collagen deposition, and liver damage, with the 0.6 mg/kg dosage exhibiting a superior effect in comparison to the 0.3 mg/kg dosage. Notably, mRNA-mediated antibody therapy offers the ability to achieve a satisfactory therapeutic effect in reversing MASH and preventing fibrosis progression with a relatively lower administered dosage (0.6 mg/kg) compared to antibody therapy alone, where systemic administration of 10 mg/kg of IL11-scFv did not demonstrate significant effects. When tested in the MASH mice with progressive fibrosis, m*IL11-scFv*@AA3G most effectively ameliorated steatosis, resolved fibrosis and inflammation, and restored liver function among all tested groups. The hepatic IL11-scFv translated from m*IL11-scFv* effectively binds to excess secreted IL-11 in the MASH liver, thereby inhibiting the IL-11 signaling pathway in hepatocytes and HSCs. This mechanism offers significant benefits for MASH therapy. The safety profile of m*IL11-scfv*@AA3G was validated in healthy C57BL/6J mice, reinforcing the promising translational potential of this mRNA-mediated targeted antibody therapy for MASH and fibrosis.

Given that IL-11 plays a critical role in hepatocyte metabolic dysfunction and HSC activation, this m*IL11-scFv*-mediated antibody therapy shows promise for other fibrotic liver diseases such as alcoholic liver disease and chronic viral hepatitis, which often share common fibrotic pathways. It should be noted that mRNA can theoretically encode any therapeutic antibody or protein; this targeted mRNA-mediated therapy can also be

https://doi.org/10.1021/acsnano.4c13404
ACS Nano XXXX, XXX, XXX−XXX

extended to cancers, infectious diseases, and other liver conditions, allowing for broad applications.

Although the current results are encouraging, our study is limited to the HFHC diet-induced early MASH model and MASH model with progressive fibrosis, which lacks investigation in different animal models (e.g., genetic mouse models) and animal species (e.g., nonhuman primates) that resemble morphologic spectrum of human MASH. Further studies are needed to comprehensively compare m*IL11-scFv*-mediated antibody therapy with siRNA therapeutics targeting the IL-11 signaling pathway in terms of off-target effects, immunogenicity, and therapeutic efficacy. These studies provide valuable insights into the application and potential translation of RNA therapeutics in MASH therapy. The extensive investigation and comparison of mRNA-encoded scFv and full-length IL-11 antibody may be included to further improve the efficacy of mRNA-mediated antibody therapy. Dose and frequency can also impact patient compliance and clinical benefit, especially for chronic diseases like MASH that require long-term treatment. Therefore, future work may focus on developing self-amplifying mRNA/circular mRNA to improve the dosing regimen.

CONCLUSIONS

In summary, we developed a safe and versatile targeting LNP platform that enables the transfer of m*IL11-scFv* to hepatic lesions for addressing MASH and related fibrosis. This mRNA-mediated liver-specific antibody therapy achieved sustained expression of IL-11 scFv antibodies in the liver and demonstrated superior therapeutic efficacy compared to systemic administration of IL-11 scFv alone. The developed targeting mRNA-LNP represents a viable platform for liver-specific antibody therapy to treat chronic liver diseases with expansion to any therapeutic antibody/protein.

EXPERIMENTAL SECTION

Materials. 1,2-Distearoyl-*sn*-glycero-3-phosphocholine (DSPC), cholesterol, 1,2-dimyristoyl-rac-glycero-3-methoxypolyethylene glycol-2000 (DMG-PEG_{2000}), and Dlin-MC3-DMA were purchased from AVT (shanghai) Pharmaceutical Tech Co., Ltd. Cy5-cholesterol was obtained from Xi'an ruixi Biological Technology Co., Ltd. Firefly luciferase mRNA was obtained from APExBIO. Citrate buffer (pH 3.0) was purchased from the Aladdin Reagent Corporation. Collagenase I and d-luciferin potassium salt were obtained from Shanghai Maokang Biotechnology Co., Ltd. Cell Counting Kit-8 was obtained from Beyotime Biotechnology.

In Vitro Transcription (IVT) of IL-11 scFv mRNA. Plasmid vectors containing the IL-11 scFv open reading frame (ORF) with a 6× His tag, 5′ untranslated region (UTR), and 3′ UTR were constructed (GENEWIZ). Plasmids were linearized with BsaI-HF (New England Biolabs) and purified using the Universal DNA Purification and Recovery Kit (TIANGEN). The resulting templates underwent IVT using the T7 RNA polymerase (Novoprotein) at 37 °C for 3 h. In this reaction, uridine-5′-triphosphate (UTP) was replaced with pseudouridine-5′-triphosphate (ΨTP, APExBIO), and CAP GAG with the structure of m7G(5′)ppp(5′)(2′-OMeA)pG was introduced. After purification with RNA Clean and Concentrator (Zymo Research), the concentration of mRNA was measured using a NanoDrop 2000 spectrophotometer (Thermo Fisher Scientific) and stored at −80 °C for future use.

Synthesis and Characterization of AA3-Dlin and DMG-PEG-GalNAc. *AA3-Dlin.* The ionizable lipid AA3-Dlin was synthesized following a previously described procedure.[30] In brief, amino alcohol (2.87 mmol) was dissolved in 5 mL of tetrahydrofuran and mixed with lipid acid at a molar ratio of 1:2. The resulting mixture was catalyzed by CALB and reacted at 60 °C for 72 h under a nitrogen atmosphere. Afterward, the CALB was removed via centrifugation, and the excess lipid acid in the supernatant was neutralized with a saturated $NaHCO_3$ solution. The mixture was extracted with ethyl acetate and dried with anhydrous $MgSO_4$ to yield a lipid ethyl acetate solution. The lipid solution was then concentrated using a rotary evaporator and dried under vacuum for subsequent use. ^{1}H NMR (400 MHz, chloroform-*d*): δ 5.45−5.23 (m, 8H), 4.19 (t, J = 5.9 Hz, 4H), 2.79−2.71 (m, 4H), 2.69−2.46 (m, 12H), 2.28 (t, J = 7.5 Hz, 4H), 2.03 (q, J = 6.9 Hz, 8H), 1.59 (t, J = 7.4 Hz, 4H), 1.37−1.22 (m, 28H), 0.91−0.82 (m, 6H).

DMG-PEG-GalNAc. Briefly, NH_2-PEG-N_3 (11.8 mg, 0.046 mmol) and *N*-(3-ammoniopropyl)-5-[3,4,6-tri-*O*-acetyl-2-acetamido-2-deoxy-*β*-D-glucopyranosyloxy]pentanamide trifluoroacetate[51] (69 mg, 0.035 mmol) were dissolved in 2 mL of DMF and stirred for 30 min at 0 °C. Then, *N*,*N*′-disuccinimidyl carbonate (100 mg, 0.162 mmol) was added at 0 °C and stirred overnight at room temperature (RT). The resulting mixture was concentrated and dissolved in triethylamine/methanol/water (1/1/1 v/v/v) followed by an overnight reaction at RT. After that, the solution was concentrated and underwent a reaction with 3-(prop-2-yn-1-yloxy)propane-1,2-diyl ditetradecanoate[52,53] (55 mg, 0.10 mmol), utilizing CuI (10 mg, 0.05 mmol) and DIEA (26 mg, 0.2 mmol) catalysts, maintained at RT overnight. The yielded DMG-PEG-GalNAc (yellow solid, 45 mg) was purified by Prep-HPLC and characterized by ^{1}H NMR (400 MHz, Chloroform-*d*). m/z cald = 2977.9 ± 44.0, found 994.0 ± n*14.7(1/3M+H^+), 999.4 ± n*14.7 [(M+NH_4^++2H^+)/3].

Preparation of mRNA-Loaded LNP Formulations. Ionizable lipids (AA3-Dlin or MC3), DSPC, cholesterol, and PEG lipids (DMG-PEG or DMG-PEG-GalNAc) were diluted in ethanol and mixed at the indicated molar percentage. The mRNA encoding luciferase or IL-11 scFv was diluted in sodium acetate buffer (pH 4.7, 25 mM). The ethanol phase and sodium acetate phase were loaded into two separate syringes at a fixed N/P ratio. The two phases were mixed in a microfluidic device (Aitesen, MPE-L2, China) at a total flow rate of 12 mL/min with a flow rate ratio of 1:3 (lipid flow rate:mRNA flow rate). The resulting solution was incubated at room temperature for 20 min and then dialyzed against PBS (pH 7.4) for 4 h to form stable mRNA-LNPs. The fresh LNP formulations were concentrated or diluted with PBS to an appropriate concentration for the studies. For Cy5-labeled LNP, a 20% molar percentage of cholesterol was replaced with Cy5-cholesterol during LNP preparation to yield fluorescently labeled LNP.

Characterization of LNP Formulations. The hydrodynamic diameter and zeta potential of LNP formulations were measured by a ZetaSizer Nano ZSE (Malvern, UK). The morphology of LNPs was characterized using TEM (Thermo Fisher Scientific, USA). mRNA encapsulation efficiency was determined by a Quant-it RiboGreen RNA Assay Kit (Invitrogen, USA). The total and free mRNA content were determined by dispersing LNPs in 1× TE buffer with or without the 2% Triton X-100, respectively. A series of RNA standard solutions and LNP samples were incubated with RiboGreen reagents (1:200 dilution) for 3 min, and the fluorescence intensity was measured with a microplate reader (excitation/emission: 480/520 nm, Tecan, Switzerland). For the stability assay, naked m*IL11-scFv* or m*IL11-scFv*@AA3G was incubated in PBS containing 10% FBS at 37 °C while being shaken to simulate physiological conditions. Samples were collected at predetermined intervals, and the encapsulated m*IL11-scFv* was extracted using 2% Triton X-100 (v/v) for electrophoresis. The particle size of the LNPs was monitored, and their aggregation state was assessed by measuring the absorbance at 660 nm.

Isolation of Liver Cells and Flow Cytometry Analysis. Liver cells were isolated through either ex vivo digestion or a modified in situ liver perfusion method, as previously described.[54,55] For ex vivo digestion, livers were excised, cut into 1−3 mm^3 pieces, and digested in 2 mg/mL collagenase I solution containing 1% (v/v) DNase at 37 °C for 30 min with shaking. Cell suspensions were filtered through a 40 μm cell strainer, harvested by centrifugation at 580 g for 5 min, and stained with antibodies for flow cytometry analysis. For in vivo digestion, C57BL/6J mice were anesthetized and underwent a laparotomy to expose the liver and inferior vena cava (IVC). Then, the IVC was cannulated, and the liver was perfused with an EGTA solution to chelate calcium and remove the blood followed by a 0.5 mg/mL collagenase I solution to dissociate the extracellular matrix. The liver

https://doi.org/10.1021/acsnano.4c13404
ACS Nano XXXX, XXX, XXX−XXX

was then removed, minced, and further digested in collagenase I solution containing 1% (v/v) DNase at 37 °C for 10 min. The cell suspensions were filtered through a 40 μm cell strainer, and red blood cells were lysed. Primary hepatocytes were collected through two centrifugation steps at 50 g for 2 min. Nonparenchymal cells (including endothelial cells, Kupffer cells, and HSCs) were collected from the supernatant by centrifugation at 580 g for 5 min before antibody staining. For cell culture, primary hepatocytes were plated onto rat tail collagen I-coated 24-well plates and incubated with a DMEM medium containing 10% FBS, 100 mg/mL streptomycin, and 100 units/mL penicillin at 37 °C in a humidified 5% CO_2 atmosphere.

The antibodies used in flow cytometry are listed as follows: PE/Cyanine7 antimouse CD45 antibody (clone 30-F11, BioLegend), Brilliant Violet 421 antimouse CD31 antibody (clone 390, BioLegend), APC/Cyanine7 antimouse/human CD11b antibody (clone M1/70, BioLegend), PE antimouse F4/80 antibody (clone BM8, BioLegend), FITC antimouse CD45 antibody (clone 30-F11, BioLegend), APC/Cyanine7 antimouse CD3 antibody (clone 17A2, BioLegend), APC antimouse/human CD11b antibody (clone M1/70, BioLegend), Alexa Fluor 700 antimouse CD8a antibody (clone 53-6.7, BioLegend), and PerCP/Cyanine5.5 antimouse Ly-6C antibody (clone HK1.4, BioLegend). The Zombie Aqua Fixable Viability Kit (catalog no. 423101) from BioLegend was used for live/dead staining at a 1:1000 dilution.

Cell Viability Assay. Primary hepatocytes were seeded into 96-well plates at a density of 5×10^3 cells per well and cultured for 24 h. Cells were treated with different LNP formulations at an mRNA concentration of 0.5 or 1.0 μg/mL for 48 h. Then, cells in each well were treated with 10 μL of a CCK8 solution and incubated for 30 min at 37 °C. The cell viability was assessed by measuring the absorbance at 450 nm using a microplate reader (Tecan, Switzerland).

Cellular Uptake Analysis. Primary hepatocytes were seeded in 24-well plates at a density of 1×10^5 cells/well and cultured at 37 °C for 24 h. Cells were treated with different Cy5-labeled LNPs at designated mRNA concentrations for 4 h. Then, cells were fixed in paraformaldehyde, stained with DAPI for 5 min, and imaged using confocal microscopy (Leica, Germany). To detect the intracellular fluorescence intensity, cells were harvested by trypsinization and resuspended in PBS for flow cytometry analysis.

Ex Vivo Imaging. In vivo distribution of different LNP formulations was studied in healthy mice or HFHC diet-induced MASH mice. Briefly, mice were intravenously injected with m*Luc*-loaded LNPs or Cy5-labeled LNPs at a dose of 3 μg of mRNA per mouse. After 6 h, the mice were intraperitoneally injected with 200 μL of d-luciferin solution (15 mg/mL) and sacrificed at 5 min postinjection for luminescence imaging. The heart, liver, spleen, lung, and kidneys were harvested and imaged with an in vivo imaging system (IVIS, PerkinElmer, USA). The pharmacokinetics of ^{Cy5}AA3G LNP were evaluated by quantifying the Cy5 fluorescence intensity in the bloodstream at predetermined time points.

In Vivo Therapeutic Studies. All animal experiments were performed with ethical compliance and approved by the Institutional Animal Care and Use Committee of Shanghai Jiao Tong University. Male C57BL/6J mice (6−8 weeks old) were obtained from the Beijing Vital River. The HFHC diet-induced MASH model was established. Briefly, mice were fed with the HFHC diet (TP2834040, TrophicDiet) supplemented with 40% kcal fat, 22% (w/w) fructose, and 2% (w/w) cholesterol for a total of 18 weeks or 24 weeks. Meanwhile, littermate mice receiving normal chow (TP2834020C1, TrophicDiet) were used as healthy controls.

For in vivo therapeutic studies, the mice were intravenously injected with different formulations once a week for a period of 4 weeks according to the administration schedules shown in Figures 4A and 5A, respectively. The mice were sacrificed 4 days after the final treatment, and blood and tissue samples were harvested for subsequent analysis. For IL-11 scFv expression and purification, HEK293 cells were transfected with PEI/m*IL11-scFv* complex at a weight ratio of 5:1 and incubated for 3 days. Then, the culture supernatant was collected and concentrated by an Amicon Ultra-2 centrifugal filter unit with an MWCO of 10 kDa. The polyhistidine-tagged IL-11 scFv protein was purified by using nickel-based immobilized metal affinity chromatography (IMAC) and subsequently concentrated in PBS (pH 7.4) for further use.

Histological Analysis. Tissue samples were fixed in 4% paraformaldehyde, embedded in paraffin, sliced into 5 μm sections, subjected to deparaffinization and rehydration processes, and finally stained with H&E, Masson's trichrome, or Sirius red using standard protocols. The expression of ACTA2 in the liver was evaluated through immunohistochemistry staining of paraffin-embedded tissues. Liver tissue sections (5 μm thickness) were processed as described above, blocked with 3% BSA, incubated with rabbit anti-ACTA2 (Servicebio), and then visualized using an HRP-conjugated antirabbit IgG detection kit (Servicebio) with a DAB peroxidase substrate. For Oil red O staining, liver tissues were embedded in O.C.T., frozen at −80 °C overnight, and then cut into 8 μm sections. The liver sections were processed with Oil red O staining according to the standard protocol. The percentages of fibrotic regions (aniline blue-stained area or Sirius red-stained area), as well as the ACTA2- or Oil red O-positive areas on stained slides, were calculated using NIH ImageJ software (Bethesda, USA). All images were observed under an optical microscope (Olympus, Japan).

Liver Hydroxyproline and Triglyceride Assay. The hydroxyproline content in the mouse liver was assessed using a hydroxyproline assay kit (Nanjing Jiancheng Bioengineering Institute, China), following the manufacturer's instructions. In brief, liver tissues were precisely weighed and homogenized followed by hydrolysis at 95 °C for 20 min. The resulting hydrolysate was then adjusted to a pH of 6.0−6.8, mixed with the appropriate amount of activated charcoal, and centrifuged at 3500 rpm for 10 min. Subsequently, the supernatant was collected and incubated with detection reagents at 60 °C for 15 min. After another centrifugation at 3500 rpm for 10 min, the resulting supernatant was added to 96-well plates for absorbance detection at 550 nm. Triglyceride levels in the liver were assessed using a Triglyceride assay kit following the manufacturer's protocol (Nanjing Jiancheng Bioengineering Institute, China).

Blood Chemistry Analysis. Both whole blood and serum were collected to evaluate the in vivo safety and therapeutic efficacy. Hematological parameters, including RBC, WBC, HGB, HCT, MCV, MCHC, and PLT, were assessed using a pocH-100iV Diff hematology analyzer (Sysmex Corporation, Japan). Biochemical parameters, including ALT, AST, ALB, TP, BUN, CRE, CK, and α-HBDH, were evaluated with commercially available kits following the manufacturer's protocol (Nanjing Jiancheng Bioengineering Institute, China). Serum β-hydroxybutyrate levels were determined using the β-hydroxybutyric acid content assay kit according to the manufacturer's guidelines (Solarbio, China).

qRT-PCR. Total RNA was extracted from mouse livers with Trizol (Invitrogen) and subsequently reverse-transcribed into cDNA using the HiScript Q RT SuperMix Kit (Vazyme). Ninety nanograms of cDNA were amplified on the CFX Opus 96 Real-Time PCR System (Bio-Rad, USA) using the ChamQ Universal SYBR qPCR Master Mix (Vazyme). The primer sequences for the qRT-PCR reactions are listed in Table S3. GAPDH served as the endogenous reference, and the data were analyzed by using the $2^{-\Delta\Delta CT}$ method.

Western Blotting. The total protein was extracted from livers with a radioimmunoprecipitation buffer containing protease inhibitors (Solarbio) and phosphatase inhibitors (Epizyme). The protein concentration was measured using an enhanced BCA protein assay kit (Beyotime). Then, the protein solution was mixed with 5× protein loading buffer and heated at 95 °C for 5 min. The samples were separated by SDS-polyacrylamide gel electrophoresis and transferred to a polyvinylidene difluoride membrane (Millipore). The membranes were blocked with 5% BSA in TBST buffer for 1 h and then incubated with primary antibodies overnight at 4 °C. The membranes were washed with TBST and further incubated with secondary antibodies for 1.5 h at room temperature followed by detection using the Omni-ECL enhanced chemiluminescence (Epizyme). Primary antibodies were mouse antiphospho-ERK 1/2 (1:1000, Santa Cruz, USA), rabbit antiphospho-JNK (1:1000, Cell Signaling Technology, USA), mouse anti-ERK 1/2 (1:1000, Santa Cruz, USA), rabbit anti-JNK (1:1000, Servicebio, China), and mouse anti-GAPDH (1:100000, Proteintech,

https://doi.org/10.1021/acsnano.4c13404
ACS Nano XXXX, XXX, XXX−XXX

China). Secondary antibodies were Goat antimouse IgG (1:5000, Proteintech, China) and Goat antirabbit IgG (1:5000, Proteintech, China).

ELISA Assay. The IL-11 scFv expression level in mouse livers was determined by an ELISA assay. Briefly, 100 ng of IL-11 protein (Genscript) was coated on 96-well ELISA plates (Jet Biofil) overnight at 4 °C, washed five times with 0.05% Tween-20 in PBS, and blocked with 5% BSA for 1 h at 37 °C. Dilutions of protein samples and standards were added to each well (100 μL per well) and incubated for 2 h at 37 °C. The plate was washed five times and incubated with monoclonal anti-6×His antibody (1:5000, Proteintech, China) for 1 h at 37 °C followed by further incubation with the secondary antibody for 1 h at room temperature. Then, the TMB substrate solution (APExBIO) was added and incubated in the dark for 10 min. H_2SO_4 (2 M) was added to stop the reaction, and the optical density was measured using a microplate reader at 450 nm.

Statistical Analysis. All statistical data are analyzed by GraphPad Prism 8.2.1 software, and results are presented as means ± standard deviation (SD). The two-tailed unpaired Student's *t* test was applied to assess statistical significance for comparisons between two groups. One-way analysis of variance (ANOVA) with post hoc Tukey test was employed to determine differences among multiple groups. A *P*-value <0.05 was considered statistically significant, and the levels of significance were indicated as follows: $*P$ <0.05, $**P$ <0.01, $***P$ <0.001, and $****P$ <0.0001.

ASSOCIATED CONTENT

Supporting Information

The Supporting Information is available free of charge at https://pubs.acs.org/doi/10.1021/acsnano.4c13404.

(Figures S1 and S2) The synthesis route of AA3-Dlin and DMG-PEG-GalNAc, (Figure S3) the ^{1}H NMR spectrum of DMG-PEG-GalNAc, (Figures S4−S7) particle size and in vivo transfection efficacy of various LNP formulations, (Figures S8 and S9) flow cytometry analysis of transfected cell subtypes, (Figures S10 and S11) characterization of m*IL11-scFv*@AA3G, (Figures S12 and S13) pharmacokinetics and antibody expression of m*IL11-scFv*@AA3G, (Figures S14 and S15) flow cytometry analysis of infiltrating hepatic inflammatory cells, (Figure S16) ELISA assay of the hepatic IL-11 expression levels in HFHC mice with indicated treatments, (Figure S17) quantitative analysis of p-JNK and p-ERK expression, (Figure S18) in vivo safety evaluation, (Table S1) characterization of different LNP formulations, (Table S2) quantitative analysis of p-JNK/JNK and p-ERK/ERK, and (Table S3) primer sequences for qRT-PCR; Table S4: *IL-11 scFv* mRNA sequences utilized in this study (PDF)

AUTHOR INFORMATION

Corresponding Authors

Xiaoyang Xu − *Department of Chemical and Materials Engineering, New Jersey Institute of Technology, Newark, New Jersey 07102, United States; Department of Biomedical Engineering, New Jersey Institute of Technology, Newark, New Jersey 07102, United States;* orcid.org/0000-0002-1634-3329; Email: xiaoyang.xu@njit.edu

Xue-Qing Zhang − *Shanghai Frontiers Science Center of Drug Target Identification and Delivery, School of Pharmaceutical Sciences, National Key Laboratory of Innovative Immunotherapy, Shanghai Jiao Tong University, Shanghai 200240, P. R. China;* orcid.org/0000-0002-4954-2586; Email: xueqingzhang@sjtu.edu.cn

Authors

Chenshuang Zhang − *Shanghai Frontiers Science Center of Drug Target Identification and Delivery, School of Pharmaceutical Sciences, National Key Laboratory of Innovative Immunotherapy, Shanghai Jiao Tong University, Shanghai 200240, P. R. China*

Yilong Teng − *Shanghai Frontiers Science Center of Drug Target Identification and Delivery, School of Pharmaceutical Sciences, National Key Laboratory of Innovative Immunotherapy, Shanghai Jiao Tong University, Shanghai 200240, P. R. China*

Xin Bai − *Shanghai Frontiers Science Center of Drug Target Identification and Delivery, School of Pharmaceutical Sciences, National Key Laboratory of Innovative Immunotherapy, Shanghai Jiao Tong University, Shanghai 200240, P. R. China*

Maoping Tang − *Shanghai Frontiers Science Center of Drug Target Identification and Delivery, School of Pharmaceutical Sciences, National Key Laboratory of Innovative Immunotherapy, Shanghai Jiao Tong University, Shanghai 200240, P. R. China*

William Stewart − *Department of Chemical and Materials Engineering, New Jersey Institute of Technology, Newark, New Jersey 07102, United States; Department of Biomedical Engineering, New Jersey Institute of Technology, Newark, New Jersey 07102, United States*

Jake Jinkun Chen − *Division of Oral Biology, School of Dental Medicine and Tufts University, Boston, Massachusetts 02111, United States; Department of Genetics, Molecular and Cell Biology, School of Medicine, Tufts University, Boston, Massachusetts 02111, United States*

Complete contact information is available at: https://pubs.acs.org/10.1021/acsnano.4c13404

Author Contributions

X.-Q.Z., X.X., and C.Z. conceived and designed the experiments. C.Z. performed most experiments. Y.T. assisted with chemical synthesis. C.Z., Y.T., X.B., M.T., J.C., X.X., and X.-Q.Z. analyzed and discussed results. C.Z., X.X., and X.-Q.Z. wrote the manuscript. X.-Q.Z., X.X., W.S., and C.Z. reviewed and edited the manuscript.

Notes

The authors declare no competing financial interest.

ACKNOWLEDGMENTS

This work was supported by the National Key Research and Development Program of China (2023YFC2606003), "Open Competition to Select the Best Candidates" Key Technology Program for Nucleic Acid Drugs of NCTIB (grant no. NCTIB2022HS02002), the Natural Science Foundation of Shanghai (23ZR1427600), the Program of Shanghai Frontiers Science Center of Drug Target Identification and Delivery (ZXWH2170101), the National Science Foundation (2001606), and the Gustavus and Louise Pfeiffer Research Foundation Award.

REFERENCES

(1) LaBrecque, D. R.; Abbas, Z.; Anania, F.; Ferenci, P.; Khan, A. G.; Goh, K. L.; Hamid, S. S.; Isakov, V.; Lizarzabal, M.; Peñaranda, M. M.; Ramos, J. F. R.; Sarin, S.; Stimac, D.; Thomson, A. B. R.; Umar, M.; Krabshuis, J.; LeMair, A.; et al. World Gastroenterology Organisation global guidelines: Nonalcoholic fatty liver disease and nonalcoholic steatohepatitis. *J. Clin. Gastroenterol.* **2014**, *48* (6), 467−473.

(2) Younossi, Z. M. Non-alcoholic fatty liver disease - A global public health perspective. *J. Hepatol.* **2019**, *70* (3), 531−544.
(3) Loomba, R.; Sanyal, A. J. The global NAFLD epidemic. *Nat. Rev. Gastroenterol. Hepatol.* **2013**, *10* (11), 686−690.
(4) Parthasarathy, G.; Revelo, X.; Malhi, H. Pathogenesis of nonalcoholic steatohepatitis: An overview. *Hepatol. Commun.* **2020**, *4* (4), 478−492.
(5) Mittal, S.; El-Serag, H. B.; Sada, Y. H.; Kanwal, F.; Duan, Z.; Temple, S.; May, S. B.; Kramer, J. R.; Richardson, P. A.; Davila, J. A. Hepatocellular carcinoma in the absence of cirrhosis in United States Veterans is associated with nonalcoholic fatty liver disease. *Clin. Gastroenterol. Hepatol.* **2016**, *14* (1), 124−131.
(6) Bedossa, P. Pathology of non-alcoholic fatty liver disease. *Liver Int.* **2017**, *37* (Suppl. 1), 85−89.
(7) Loomba, R.; Friedman, S. L.; Shulman, G. I. Mechanisms and disease consequences of nonalcoholic fatty liver disease. *Cell* **2021**, *184* (10), 2537−2564.
(8) Romero, F. A.; Jones, C. T.; Xu, Y.; Fenaux, M.; Halcomb, R. L. The race to bash NASH: Emerging targets and drug development in a complex liver disease. *J. Med. Chem.* **2020**, *63* (10), 5031−5073.
(9) Friedman, S. L.; Neuschwander-Tetri, B. A.; Rinella, M.; Sanyal, A. J. Mechanisms of NAFLD development and therapeutic strategies. *Nat. Med.* **2018**, *24* (7), 908−922.
(10) Ipsen, D. H.; Lykkesfeldt, J.; Tveden-Nyborg, P. Molecular mechanisms of hepatic lipid accumulation in non-alcoholic fatty liver disease. *Cell. Mol. Life Sci.* **2018**, *75* (18), 3313−3327.
(11) Gluchowski, N. L.; Becuwe, M.; Walther, T. C.; Farese, R. V. Lipid droplets and liver disease: From basic biology to clinical implications. *Nat. Rev. Gastroenterol. Hepatol.* **2017**, *14* (6), 343−355.
(12) Neuschwander-Tetri, B. A. Hepatic lipotoxicity and the pathogenesis of nonalcoholic steatohepatitis: The central role of nontriglyceride fatty acid metabolites. *Hepatology* **2010**, *52* (2), 774−788.
(13) Rector, R. S.; Thyfault, J. P.; Uptergrove, G. M.; Morris, E. M.; Naples, S. P.; Borengasser, S. J.; Mikus, C. R.; Laye, M. J.; Laughlin, M. H.; Booth, F. W.; et al. Mitochondrial dysfunction precedes insulin resistance and hepatic steatosis and contributes to the natural history of non-alcoholic fatty liver disease in an obese rodent model. *J. Hepatol.* **2010**, *52* (5), 727−736.
(14) Dong, J.; Viswanathan, S.; Adami, E.; Singh, B. K.; Chothani, S. P.; Ng, B.; Lim, W. W.; Zhou, J.; Tripathi, M.; Ko, N. S. J.; Shekeran, S. G.; Tan, J.; Lim, S. Y.; Wang, M.; Lio, P. M.; Yen, P. M.; Schafer, S.; Cook, S. A.; Widjaja, A. A.; et al. Hepatocyte-specific IL11 cis-signaling drives lipotoxicity and underlies the transition from NAFLD to NASH. *Nat. Commun.* **2021**, *12* (1), 66.
(15) He, Y.; Hwang, S.; Ahmed, Y. A.; Feng, D.; Li, N.; Ribeiro, M.; Lafdil, F.; Kisseleva, T.; Szabo, G.; Gao, B. Immunopathobiology and therapeutic targets related to cytokines in liver diseases. *Cell. Mol. Immunol.* **2021**, *18* (1), 18−37.
(16) Widjaja, A. A.; Singh, B. K.; Adami, E.; Viswanathan, S.; Dong, J.; D'Agostino, G. A.; Ng, B.; Lim, W. W.; Tan, J.; Paleja, B. S.; Tripathi, M.; Lim, S. Y.; Shekeran, S. G.; Chothani, S. P.; Rabes, A.; Sombetzki, M.; Bruinstroop, E.; Min, L. P.; Sinha, R. A.; Albani, S.; Yen, P. M.; Schafer, S.; Cook, S. A.; et al. Inhibiting interleukin 11 signaling reduces hepatocyte death and liver fibrosis, inflammation, and steatosis in mouse models of nonalcoholic steatohepatitis. *Gastroenterology* **2019**, *157* (3), 777−792.
(17) Zhang, C.; Teng, Y.; Li, F.; Ho, W.; Bai, X.; Xu, X.; Zhang, X.-Q. Nanoparticle-mediated RNA therapy attenuates nonalcoholic steatohepatitis and related fibrosis by targeting activated hepatic stellate cells. *ACS Nano* **2023**, *17* (15), 14852−14870.
(18) Carter, P. J.; Lazar, G. A. Next generation antibody drugs: pursuit of the 'high-hanging fruit'. *Nat. Rev. Drug Discovery* **2018**, *17* (3), 197−223.
(19) Tsumoto, K.; Isozaki, Y.; Yagami, H.; Tomita, M. Future perspectives of therapeutic monoclonal antibodies. *Immunotherapy* **2019**, *11* (2), 119−127.
(20) Rohner, E.; Yang, R.; Foo, K. S.; Goedel, A.; Chien, K. R. Unlocking the promise of mRNA therapeutics. *Nat. Biotechnol.* **2022**, *40* (11), 1586−1600.
(21) Kubiatowicz, L. J.; Mohapatra, A.; Krishnan, N.; Fang, R. H.; Zhang, L. mRNA nanomedicine: Design and recent applications. *Exploration* **2022**, *2* (6), No. 20210217.
(22) Zhang, M.; Hussain, A.; Yang, H.; Zhang, J.; Liang, X.-J.; Huang, Y. mRNA-based modalities for infectious disease management. *Nano Res.* **2023**, *16* (1), 672−691.
(23) Huang, X.; Kong, N.; Zhang, X.; Cao, Y.; Langer, R.; Tao, W. The landscape of mRNA nanomedicine. *Nat. Med.* **2022**, *28* (11), 2273−2287.
(24) Baden, L. R.; El Sahly, H. M.; Essink, B.; Kotloff, K.; Frey, S.; Novak, R.; Diemert, D.; Spector, S. A.; Rouphael, N.; Creech, C. B.; McGettigan, J.; Khetan, S.; Segall, N.; Solis, J.; Brosz, A.; Fierro, C.; Schwartz, H.; Neuzil, K.; Corey, L.; Gilbert, P.; Janes, H.; Follmann, D.; Marovich, M.; Mascola, J.; Polakowski, L.; Ledgerwood, J.; Graham, B. S.; Bennett, H.; Pajon, R.; Knightly, C.; Leav, B.; Deng, W.; Zhou, H.; Han, S.; Ivarsson, M.; Miller, J.; Zaks, T.; et al. Efficacy and safety of the mRNA-1273 SARS-CoV-2 vaccine. *N. Engl. J. Med.* **2021**, *384* (5), 403−416.
(25) Wang, X. Safety and efficacy of the BNT162b2 mRNA Covid-19 vaccine. *N. Engl. J. Med.* **2021**, *384* (16), 1576−1577.
(26) Mendes, B. B.; Conniot, J.; Avital, A.; Yao, D.; Jiang, X.; Zhou, X.; Sharf-Pauker, N.; Xiao, Y.; Adir, O.; Liang, H.; Shi, J.; Schroeder, A.; Conde, J.; et al. Nanodelivery of nucleic acids. *Nat. Rev. Methods Primers* **2022**, *2*, 1−21.
(27) Ma, Y.; Li, S.; Lin, X.; Chen, Y. A perspective of lipid nanoparticles for RNA delivery. *Exploration* **2024**, *4*, No. 20230147.
(28) Liu, R.; Luo, C.; Pang, Z.; Zhang, J.; Ruan, S.; Wu, M.; Wang, L.; Sun, T.; Li, N.; Han, L.; et al. Advances of nanoparticles as drug delivery systems for disease diagnosis and treatment. *Chin. Chem. Lett.* **2023**, *34* (2), No. 107518.
(29) Chen, L.; Liu, Y.; Guo, W.; Liu, Z. Light responsive nucleic acid for biomedical application. *Exploration* **2022**, *2*, No. 20210099.
(30) Li, Z.; Zhang, X.-Q.; Ho, W.; Li, F.; Gao, M.; Bai, X.; Xu, X. Enzyme-catalyzed one-step synthesis of ionizable cationic lipids for lipid nanoparticle-based mRNA COVID-19 vaccines. *ACS Nano* **2022**, *16* (11), 18936−18950.
(31) Li, F.; Zhang, X. Q.; Ho, W.; Tang, M.; Li, Z.; Bu, L.; Xu, X. mRNA lipid nanoparticle-mediated pyroptosis sensitizes immunologically cold tumors to checkpoint immunotherapy. *Nat. Commun.* **2023**, *14* (1), 4223.
(32) Sedic, M.; Senn, J. J.; Lynn, A.; Laska, M.; Smith, M.; Platz, S. J.; Bolen, J.; Hoge, S.; Bulychev, A.; Jacquinet, E.; et al. Safety evaluation of lipid nanoparticle-formulated modified mRNA in the sprague-dawley rat and cynomolgus monkey. *Vet. Pathol.* **2018**, *55* (2), 341−354.
(33) Padín-González, E.; Lancaster, P.; Bottini, M.; Gasco, P.; Tran, L.; Fadeel, B.; Wilkins, T.; Monopoli, M. P. Understanding the role and impact of poly (ethylene glycol) (PEG) on nanoparticle formulation: implications for COVID-19 vaccines. *Front. Bioeng. Biotechnol.* **2022**, *10*, No. 882363.
(34) Mui, B. L.; Tam, Y. K.; Jayaraman, M.; Ansell, S. M.; Du, X.; Tam, Y. Y. C.; Lin, P. J.; Chen, S.; Narayanannair, J. K.; Rajeev, K. G.; et al. Influence of polyethylene glycol lipid desorption rates on pharmacokinetics and pharmacodynamics of siRNA lipid nanoparticles. *Mol. Ther. Nucleic Acids* **2013**, *2* (12), No. e139.
(35) Huang, C.; Duan, X.; Wang, J.; Tian, Q.; Ren, Y.; Chen, K.; Zhang, Z.; Li, Y.; Feng, Y.; Zhong, K.; Wang, Y.; Zhou, L.; Guo, G.; Song, X.; Tong, A.; et al. Lipid nanoparticle delivery system for mRNA encoding B7H3-redirected bispecific antibody displays potent antitumor effects on malignant tumors. *Adv. Sci.* **2023**, *10* (3), No. e2205532.
(36) Pardi, N.; Hogan, M. J.; Porter, F. W.; Weissman, D. mRNA vaccines - a new era in vaccinology. *Nat. Rev. Drug Discovery* **2018**, *17* (4), 261−279.
(37) Gauduin, M.-C.; Parren, P. W. H. I.; Weir, R.; Barbas, C. F.; Burton, D. R.; Koup, R. A. Passive immunization with a human

https://doi.org/10.1021/acsnano.4c13404
ACS Nano XXXX, XXX, XXX−XXX

monoclonal antibody protects hu-PBL-SCID mice against challenge by primary isolates of HIV-1. *Nat. Med.* **1997**, *3*, 1389−1393.
(38) Kumar Srivastava, A.; Khare, P.; Kumar Nagar, H.; Raghuwanshi, N.; Srivastava, R. Hydroxyproline: A potential biochemical marker and its role in the pathogenesis of different diseases. *Curr. Protein Pept. Sci.* **2016**, *17* (6), 596−602.
(39) Wu, G.; Bazer, F. W.; Burghardt, R. C.; Johnson, G. A.; Kim, S. W.; Knabe, D. A.; Li, P.; Li, X.; McKnight, J. R.; Satterfield, M. C.; et al. Proline and hydroxyproline metabolism: implications for animal and human nutrition. *Amino Acids* **2011**, *40* (4), 1053−1063.
(40) Pellicoro, A.; Ramachandran, P.; Iredale, J. P.; Fallowfield, J. A. Liver fibrosis and repair: Immune regulation of wound healing in a solid organ. *Nat. Rev. Immunol.* **2014**, *14* (3), 181−194.
(41) Ekstedt, M.; Hagström, H.; Nasr, P.; Fredrikson, M.; Stål, P.; Kechagias, S.; Hultcrantz, R. Fibrosis stage is the strongest predictor for disease-specific mortality in NAFLD after up to 33 years of follow-up. *Hepatology* **2015**, *61* (5), 1547−1554.
(42) Konerman, M. A.; Jones, J. C.; Harrison, S. A. Pharmacotherapy for NASH: Current and emerging. *J. Hepatol.* **2018**, *68* (2), 362−375.
(43) Harrison, S. A.; Loomba, R.; Dubourg, J.; Ratziu, V.; Noureddin, M. Clinical trial landscape in NASH. *Clin. Gastroenterol. Hepatol.* **2023**, *21* (8), 2001−2014.
(44) Xu, X.; Poulsen, K. L.; Wu, L.; Liu, S.; Miyata, T.; Song, Q.; Wei, Q.; Zhao, C.; Lin, C.; Yang, J. Targeted therapeutics and novel signaling pathways in nonalcohol-associated fatty liver/steatohepatitis (NAFL/NASH). *Signal Transduction Targeted Ther.* **2022**, *7* (1), 287.
(45) Safdari, Y.; Ahmadzadeh, V.; Khalili, M.; Jaliani, H. Z.; Zarei, V.; Erfani-Moghadam, V. Use of single-chain antibody derivatives for targeted drug delivery. *Mol. Med.* **2016**, *22*, 258−270.
(46) Muñoz-López, P.; Ribas-Aparicio, R. M.; Becerra-Báez, E. I.; Fraga-Pérez, K.; Flores-Martínez, L. F.; Mateos-Chávez, A. A.; Luria-Pérez, R. Single-chain fragment variable: recent progress in cancer diagnosis and therapy. *Cancers* **2022**, *14* (17), 4206.
(47) Setten, R. L.; Rossi, J. J.; Han, S.-P. The current state and future directions of RNAi-based therapeutics. *Nat. Rev. Drug Discovery* **2020**, *19* (4), 290.
(48) Hu, B.; Zhong, L.; Weng, Y.; Peng, L.; Huang, Y.; Zhao, Y.; Liang, X. J. Therapeutic siRNA: state of the art. *Signal Transduction Targeted Ther.* **2020**, *5* (1), 101.
(49) Springer, A. D.; Dowdy, S. F. GalNAc-siRNA conjugates: Leading the way for delivery of RNAi therapeutics. *Nucleic Acid Ther.* **2018**, *28* (3), 109−118.
(50) Debacker, A. J.; Voutila, J.; Catley, M.; Blakey, D.; Habib, N. Delivery of oligonucleotides to the liver with GalNAc: From research to registered therapeutic drug. *Mol. Ther.* **2020**, *28* (8), 1759−1771.
(51) Maklakova, S. Y.; Kucherov, F. A.; Petrov, R. A.; Gopko, V. V.; Shipulin, G. A.; Zatsepin, T. S.; Beloglazkina, E. K.; Zyk, N. V.; Majouga, A. G.; Koteliansky, V. E. A new approach to the synthesis of ligands of asialoglycoprotein receptor for targeted delivery of oligonucleotides to hepatocytes. *Russ. Chem. Bull.* **2015**, *64* (7), 1655−1662.
(52) Reise, F.; Warias, J. E.; Chatterjee, K.; Krekiehn, N. R.; Magnussen, O.; Murphy, B. M.; Lindhorst, T. K. Photoswitchable glycolipid mimetics: Synthesis and photochromic properties of glycoazobenzene amphiphiles. *Chemistry* **2018**, *24* (66), 17497−17505.
(53) Gao, M.; Li, Y.; Ho, W.; Chen, C.; Chen, Q.; Li, F.; Tang, M.; Fan, Q.; Wan, J.; Yu, W.; et al. Targeted mRNA nanoparticles ameliorate blood−brain barrier disruption postischemic stroke by modulating microglia polarization. *ACS Nano* **2024**, *18* (4), 3260−3275.
(54) Zhang, Q.; Qu, Y.; Li, Z.; Zhang, Q.; Xu, M.; Cai, X.; Li, F.; Lu, L. Isolation and culture of single cell types from rat liver. *Cells Tissues Organs* **2016**, *201* (4), 253−267.
(55) Mederacke, I.; Dapito, D. H.; Affò, S.; Uchinami, H.; Schwabe, R. F. High-yield and high-purity isolation of hepatic stellate cells from normal and fibrotic mouse livers. *Nat. Protoc.* **2015**, *10* (2), 305−315.

https://doi.org/10.1021/acsnano.4c13404
ACS Nano XXXX, XXX, XXX−XXX